Spin Electronic Devices – Combine the Hard Disk and the Processor

Alex Valavanis
University of York

June 2004

4th Year Project Report for degree of MEng in Electronic Engineering

Abstract

Spintronics is a new field in which both spin and charge of carriers are exploited. This leads to new devices as well as enhancement of current technology. The underlying physical principles and realisable applications are examined. It is shown that resonance at microwave frequencies will minimise the electrical resistance and allow clearer observation of magnetoresistance.

Practical work covers the design and fabrication of a hybrid spin-valve using a GaAs channel. Contacts of permalloy and cobalt are used to achieve independent switching of magnetization. Measurements confirm a good schottky barrier and 14% magnetoresistance ratio at room temperature.

Table of Contents

Table of Figures

1 Acknowledgements

Over the past six months, I have received assistance and encouragement from a number of people. Without them, the success of this project would have been severely restricted and I thank them all sincerely for all they have done.

Firstly, I would like to thank my supervisors, Dr Yongbing Xu and Prof Mohammed El-Gomati for introducing me to the fascinating field of Microelectronics and then further into the exciting new research area of Spintronics. It has been a privilege to work, albeit briefly, at the "cutting edge" of technology.

My practical work has been aided by several of the Experimental and Technical staff. In particular, Malcolm Law, Iain Will, Jonathan Cremer and Torquil Wells – all of whom helped to point me in the right direction on numerous occasions and helped to repair the damage on a few others!

Fellow members of the Spintronics Research Group have provided much advice and encouragement. I have been honoured to have the guidance of Dr Ehsan Ahmad, whose expertise in practical development of Spin-transport devices has been an inspiration to me. I am grateful for the help of Yongxiong Lu for assistance with MOKE measurements and Jill Claydon for finding several useful papers on this subject. In other research groups, I am particularly grateful for the help of Tim Clarke and James Carmichael who have acted as my guides in MATLAB programming and Dr Stuart Porter, Dr Myles Capstick and Prof Jeremy Everard who have helped me gain an insight into the twilight area between Spintronics and Electromagnetics. I am also grateful for the encouragement of my friends and family who tolerated my "overtime" and the long, stimulating descriptions of my work on several occasions without complaint. In particular, I am grateful to James Telfer for proof reading this report and for his continuous support and friendship.

Alex Valavanis
York, June 2004

"As change quickens, our need grows"

- K. Eric Drexler[1]

"These are exciting times for participants and spectators alike as an era of creativity, ultimately unleashed by the earlier mastery of electromagnetism continues to unfold"

- M R Freeman & B C Choi[2]

2 An Introduction to Spintronics

2.1 The Limits of Miniaturisation

Advances in the field of Microelectronics are fundamental to the development of new electronic devices and systems. A classic example of this is computer systems design, where consumer demand and industry competition requires that devices become constantly faster and more intelligent than the previous generation. Industry aims to follow “Moore’s Law”, which predicts that the integration densities of integrated circuits (ICs) will double every year[3]. The approach of consistently reducing the size of devices has worked well, with densities currently doubling around every 18 months (slightly less than Moore’s prediction). However, the cost of fabrication has increased dramatically. The original photolithographic methods used for developing ICs were relatively simple. A set of photo masks was constructed by scaling down an IC layout design to the desired proportions. As the dimensions of patterns have reduced, the designs of masks have become much more complex, requiring methods such as Optical Proximity Correction and Phase-Shift Masking (PSM) and typical mask sets now cost in the region of $500,000[4]. Recent methods such as electron-beam or dip-pen lithography[5] provide smaller features but are much slower.

The miniaturisation approach also has a fundamental limit, as stable matter must obviously be used to produce commercial devices. In other words, it is not feasible to use sub-nucleonic particles in their construction. Atomic-scale devices using single electrons have already been demonstrated[6], and therefore a “brick-wall” will very soon be reached. Some estimates of the timing of this event lie as close as 2010[7]. Thus, the onus is now upon the development of devices with more degrees of freedom than those currently available. Ideas such as quantum computing, where particles display a superposition of quantum states rather than one of a binary pair, will allow vastly increased efficiency in computation without the need for more costly size-reduction steps.

2.2 The Advantages of Spintronics

This project will investigate another paradigm for improving computer system efficiency – that of Spintronics, an emerging field that aims to exploit the quantum spin properties of electrons in addition to their charge properties in order to add a degree of freedom to device operation. Spintronics has evolved from several other areas of Electronics including Nanotechnology, Photonics and Magnetics. Spintronic devices are designed to use the magnetic properties of the carriers as an additional control method to their charge properties. The excitement surrounding Nanotechnology and hence Spintronics is shared by theorists, experimentalists and industry alike. Indeed, the research budget for Nanotechnology in the US is currently third only to biomedical research and defence and rising extremely rapidly by around $200M per year[8]. The advantages of Spintronic devices over purely charge-based devices are many. The energy required to modify the spin-polarization of a current is generally lower than that lost in resistive interactions in materials and hence the power dissipation of Spintronic devices is lower. In other words, spin-based devices are more efficient and amenable to high integration densities. Certain Spintronic devices contain nanoscale magnetic elements making them ideal as non-volatile high-density data-storage units. Spintronics has also led to the proposal of several active devices such as the spin-based field effect transistor (Spin-FET). Such a transistor would be reconfigurable by the application of a magnetic field, allowing an extra degree of freedom to the device. Spintronic devices may prove to be compatible with quantum computing paradigms in that a carrier may display a superposition of spin states. This would lead to the development of highly efficient microprocessors and other digital devices, combining the functions of two or more conventional computer components.

2.3 Project Aims and Report Structure

This project aims to establish strong theoretical and experimental evidence for the spin-transport properties required to construct spin-FETs. In order to demonstrate these properties experimentally, hybrid spin-valves (section 4.5) were fabricated using a variety of geometries and measurements were performed to test their magnetic and electrical properties.

An analysis of the Physical principles behind Spintronics and a number of common device structures are used to justify the design decisions made in the following section. Prior to a description of the practical work undertaken, a diversion is made to explore in greater depth the effect of Spintronics upon communications systems and upon programmable logic devices.

The description of the practical work itself is divided into two sections. The first gives a detailed description of the preliminary investigations into the techniques, equipment and materials used in fabricating the hybrid spin-valve. Techniques including trial fabrications, and Magneto-optic Kerr Effect (MOKE) measurements were used to confirm the feasibility of the design. Details of the fabrication of several hybrid spin-valves are given in the second section along with the electrical and magnetic measurements performed.

In the final sections of the report, conclusions and recommendations for further work are made. Appendices describe the MATLAB simulations and mathematical derivations used in the project in detail. A glossary of abbreviations and a list of references are given at the end.

3 A Review of the Physics of Magnetism in Materials

3.1 Spin

A material's magnetization is defined as the *vector sum of all the magnetic dipole moments of the atoms per unit volume.* The orbit of an electron around the nucleus of an atom is effectively a current loop and hence has an associated magnetic moment perpendicular to the loop. In addition, the electrons possess a property called spin. This is similar to the classical model of a charged body spinning on its axis, except it is important to note that the electron is governed by Quantum Physics and the charged body model is only an illustration of this concept. In fact, a classical model of the electron would have to rotate faster than the speed of light to produce the observed magnetization due to quantum spin effects. Thus, spin is a quantum property with readily observed macroscopic effects within materials.

3.2 Paramagnetism and Diamagnetism

In materials described as paramagnetic, their magnetization is primarily due to electron spin effects[9] [10]. This induces a magnetic field aligned to an externally applied magnetic field.

In diamagnetic materials however, it is the orbital motion of electrons, which contributes to the magnetization. This induces a magnetic field in the opposite direction to that of an eternally applied magnetic field.

3.3 Ferromagnetism

This behaviour is demonstrated by materials such as iron, nickel, cobalt and their alloys. In this case, neighbouring atoms have strongly coupled magnetic moments and hence areas called "magnetic domains" exist in which most atoms have parallel magnetic moments. Therefore, permanent magnetization is possible where the vector sum of domain alignments is non-zero. In fact, for ferromagnetic materials the parallel alignment of domains is so stable that even after the removal of the external field there is a residual magnetization present in the material called the "reminance." In order to reduce this residual magnetization to zero, an external magnetic field must be applied in the opposite direction. The size of this reverse field is called the "coercivity." Above a particular size of external field in either direction, the magnetization remains constant. This effect, known as "saturation", is due to the magnetic domains becoming aligned with each other and offering their maximum contribution to the magnetization vector. These properties lead to the relationship between the applied magnetic field and magnetization of the material being hysteretic i.e. the magnetization is dependent on the history of the material's magnetization as well as the applied magnetic field. A typical hysteresis plot is shown below.

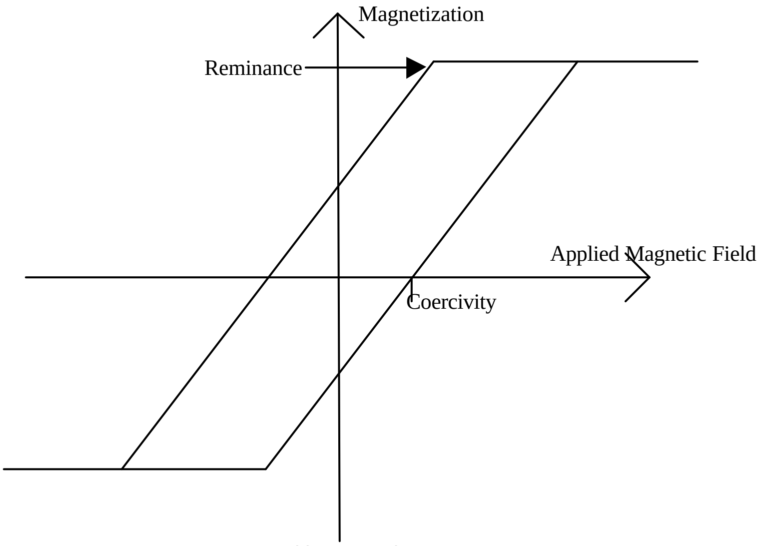

One can distinguish between different ferromagnetic materials in terms of the ease with which they are magnetized. A *hard ferromagnetic material* has a very large coercivity and saturation field whereas the converse applies for a *soft ferromagnetic material*. In addition, *magnetic anisotropy* may be observed, where the magnetization properties vary depending on the direction of the applied magnetic field. This means that in a particular magnetic field direction known as the *easy axis*, the material displays a relatively low coercivity whereas in the orthogonal direction, known as the *hard axis*, the coercivity is high. Magnetic anisotropy may be caused by a number of factors, including the crystal structure and orientation or the shape of the bulk of material. For some epitaxially grown materials, the anisotropic effects may be considerable[11,12].

Ferromagnetic materials are distinguished from paramagnetic and diamagnetic materials by their energy band structure. The densities of states at the Fermi level are different for particles with up or down spins due to spin-dependent splitting of the energy bands[13]. This means that at equilibrium, a non-zero magnetization exists in ferromagnetic materials.

Further to this, it can be shown that the bulk conductivity of the material is dependent upon the spin-polarization of the current relative to the magnetization.

3.4 The Hall Effect

A result of Maxwell's Equations is that a moving charged particle is subject to a force, which depends on both the applied electric and magnetic fields[14]. The electric field accelerates carriers as shown in Equation 1 where q is the charge on a carrier and $\mathbf{E}$ is the applied electric field. For electrons, the charge is negative so the force will act in a direction opposite to the electric field. For holes, the force will act parallel to the electric field.

$$\text{Electric Force} = \mathbf{F_e} = q\mathbf{E}$$

Equation 1: Electric Force Equation

An applied magnetic field however does no work on the carriers, it merely "steers" them according to Equation 2 where $\mathbf{B}$ is the magnetic flux density and $\mathbf{u}$ is the velocity of the carrier. This means that all carriers in the material will be steered towards one edge of the material. The holes and electrons are diverted in the same direction, as their velocity vectors are opposed as well as their charges thus yielding the same force.

$$\text{Magnetic Force} = \mathbf{F_m} = q(\mathbf{u} \times \mathbf{B})$$

Equation 2: Magnetic Force Equation

This effect is shown diagrammatically in Figure 1, where the carriers travel in opposite directions (collinear with the electric field vector) and are diverted in the same direction, and perpendicular to the direction of travel and to the magnetic field vector.

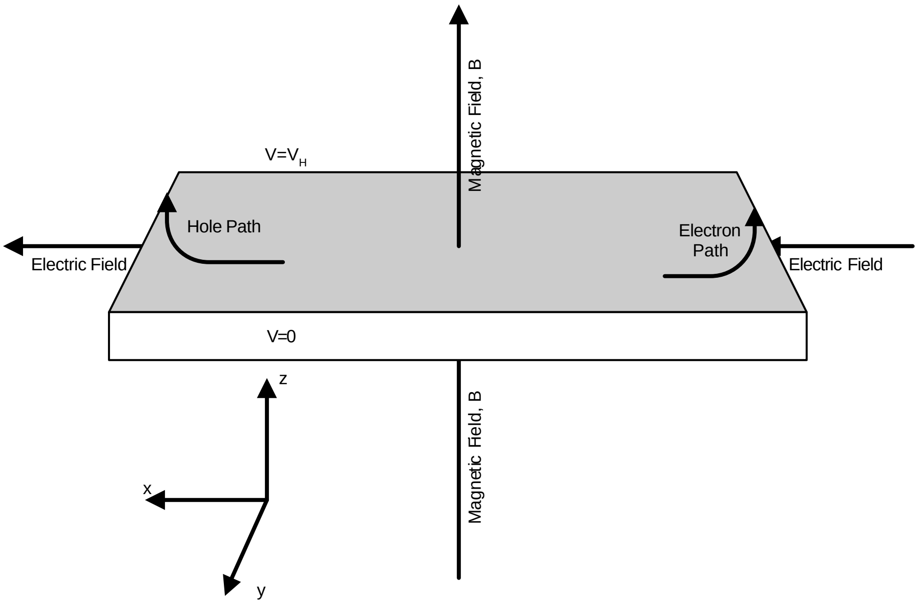

Figure 1: The Hall Effect

The total force on a carrier is therefore the sum of the electric and magnetic forces, known as the *Lorenz Force*.

$$\mathbf{F} = \mathbf{F_e} + \mathbf{F_m} = q\mathbf{E} + q(\mathbf{u} \times \mathbf{B}) = q(\mathbf{E} + \mathbf{u} \times \mathbf{B})$$

Equation 3: The Lorenz Force

In a material where hole and electron densities are approximately equal, the net charge at the edge of the material is zero and no noticeable effect occurs. However, in a material with uneven densities of carriers such as an n-type semiconductor, the charge separation can be large. This charge separation leads to the existence of an electric field component from the side with net positive charge to the side with net negative charge. This field increases until the point where it opposes the magnetic force completely i.e. where:

$$\begin{aligned}
&\hat{\mathbf{y}} \cdot \mathbf{E} = -\hat{\mathbf{y}} \cdot (\mathbf{u} \times \mathbf{B}) \\
&\Rightarrow E_y = -\mathbf{u} \cdot (\mathbf{B} \times \hat{\mathbf{y}}) \\
&\Rightarrow E_y = \mathbf{u} \cdot (\hat{\mathbf{x}} B) \\
&\Rightarrow E_y = u_x B
\end{aligned}$$

The presence of this electric field yields a voltage in the opposite direction, defined as the *Hall Voltage*, V_H (Equation 4) where y is the width of the material in the **y** direction.

$$\begin{aligned} V_H &= E_y y \\ \Rightarrow V_H &= Buy \end{aligned}$$

Equation 4: Hall Voltage Definition

In addition, the current is given by $I = nyzuq$[15], where n is the carrier density and z is the height of the material in the **z** direction. This can be combined with the Hall voltage definition to yield Equation 5:

$$V_H = \frac{BIy}{nyzq} = \frac{BI}{nzq}$$

Equation 5: Hall Voltage Equation

3.5 The Magneto-Optic Kerr Effect (MOKE)

The Magneto-Optic Kerr Effect is a useful property of magnetic materials, which results in the rotation of polarizations of photons incident upon a magnetised material[2]. This property is exploited in magnetic measurements by directing a plane-polarized monochromatic laser beam onto a magnetic material and observing the polarization of the reflected beam. When the sample is demagnetized, the reflected beam has the same polarization as the incident beam whilst beams reflected from magnetized materials exhibit a rotation of polarization related to the magnetization vector.

A simplified top down diagram of the experimental apparatus is shown in Figure 2.

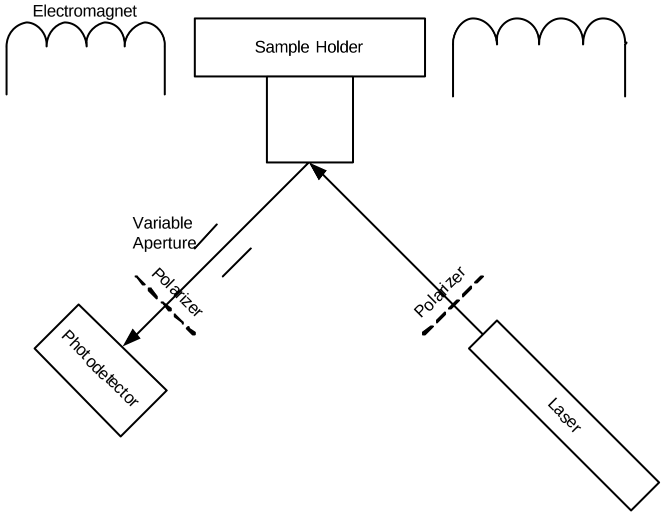

Figure 2: Top down View of MOKE measurement Equipment

The incident beam is passed through an optical polarizer and the position of the sample is adjusted with three positioning screws such that the reflected beam hits the detector. The reflected beam passes through an aperture, which is adjusted to give the optimal optical intensity at the detector for low-noise measurements. The beam then passes through a second, identically oriented polarizer. The detected light intensity therefore varies from the initial value to zero as the polarization of the light is rotated.

An electromagnet is placed around the sample holder such that the magnetic field is directed parallel to the face of the sample. The current source supplying the magnet is controlled by a computer.

The output voltage from the detector is monitored by the computer at a predetermined set of discrete magnetic field strengths. The field is swept in both an upward and downward direction so that the full hysteresis loop for a ferromagnetic material is tested and a graph of MOKE voltage against applied magnetic field is generated. A number of sweeps may be performed and then averaged to produce a less noisy final graph. The result is a graph bearing the same shape as the hysteresis loop for the material.

A simplified diagram of the front view of the sample holder is shown in Figure 3.

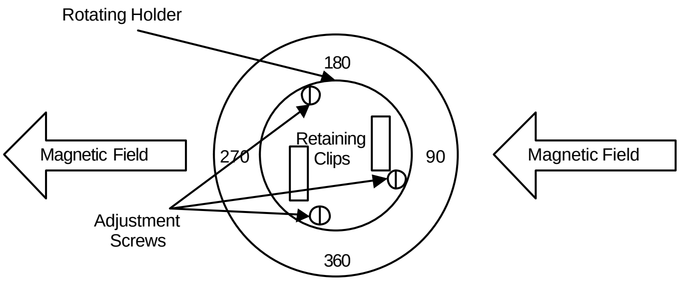

Figure 3: Simplified Front View of Sample Holder in MOKE Equipment

The sample itself is held in place with the aid of two retaining clips. Its position is adjusted by three screws. The holder has an angular scale through 360 degrees at its periphery. The holder may be rotated freely to align the sample in any direction with respect to the applied magnetic field. In this way, the sample's magnetic characteristics may be observed in a number of different field directions and magnetic anisotropy may be investigated.

3.6 Spin Injection

In section 3.3, the spin-dependent conductivity of ferromagnetic materials was described. However, in Spintronic devices it is also desirable to achieve a spin-polarized current in nonmagnetic materials such as GaAs. In terms of practical devices, in which a ferromagnet is connected to a nonmagnetic material, the current may be passed across the interface in one of two ways.

3.6.1 Ohmic Injection

Firstly, an ohmic contact may be used as the interface. This has proved somewhat difficult in practice, as the conductivity mismatch between the two materials is generally very significant. In addition, the cleanliness of the interface will lead to scattering of carriers and degrade the spin-polarization of the current[46]. This report proposes an investigation into the effect of microwave impedance matching upon spin-injection across a ferromagnetic metal-semiconductor interface.

3.6.2 Tunnelling Injection

The second method is the use of a tunnelling junction between the two materials. In this case, it is the interface, which determines the injection properties rather than the bulk material. Indeed, work by E I Rashba (the discoverer of the Rashba Effect) suggests that the use of a tunnelling junction would solve the problems caused by conductivity mismatch[16]. The use of a dielectric such as Al_2O_3 at the interface has been investigated although the formation of pinholes between the metallic layers is a serious problem[31]. Other experimental data shows that tunnelling through a schottky barrier between a ferromagnetic metal and a highly doped semiconductor yields spin injection of up to 32%[17]. As schottky barriers are well established in semiconductor fabrication technology, this would appear to be a very promising method for achieving spin-injection.

3.6.3 Optical Injection

Regardless of the debate over which method of spin injection should be used in commercial Spintronic devices, one must recognize that this is only one aspect of the quest for a practical device. As such, another method is used to create a net spin-polarization in devices thus allowing spin transport phenomena and other aspects of device operation to be investigated. The use of a circularly polarised laser, incident upon a semiconductor material encourages carriers with a particular spin orientation to form through generation of electron-hole pairs. Whilst this method allows a good level of spin injection into the device without the need for a ferromagnetic injector contact, the cost and size of lasers makes it completely impractical for integration.

By a similar process, photon emissions in a quantum well in a direct gap semiconductor such as GaAs exhibit a level of circular polarization related to the spin-polarization of the current in the region[31]. Using this principle, quantum-wells are sometimes incorporated into Spintronic devices for testing spin-injection. Such devices are often referred to as spin-based light-emitting diodes (spin-LED).

3.7 Spin Transport

As a starting point for this discussion, the analogy with pure charge-based devices will be used. In order for a device to operate correctly, it is essential that sufficient useful carriers are able to travel across the material to be detected at the output. The carriers contribute to the charge conductivity of the material when electrons are excited from the valence band of a semiconductor to the conduction band. In this state, an applied electric field will create a net motion of charge.

Electrons have a probability of recombining with holes i.e. “falling” back to the valence band. In doing this, energy is released and the carriers no longer contribute to the charge transport in the material. This probability of an electron and hole recombining is characterised by a *carrier lifetime*, which is the decay constant for carrier concentrations, t[18]. Due to intrinsic random motion of particles in a system, carriers tend to diffuse in the direction of a negative concentration gradient. The rate of diffusion is related to the negative concentration gradient by a proportionality constant called the *diffusion coefficient, D* It can then be shown that the concentration of carriers over a length of semiconductor material decays exponentially with a decay constant called the *diffusion length, L*. The value of this constant is related to the diffusion coefficient and the carrier lifetime by Equation 6.

$$L_{n,p} = \sqrt{D_{n,p} t_{n,p}}$$

Equation 6: Diffusion Length for Pure Charge Transport

It is important therefore, that in the design of charge-based devices, the channel lengths for carriers are compared to the diffusion length.

Much work has been done on the spin-transport properties of carriers through materials. As carriers move through a non-magnetic material, the spin-polarization decays in a process known as spin relaxation. One may begin by assuming that a population of carriers with up spin only, is injected into a semiconductor.

As the carriers move, they interact weakly with the material and lose a small amount of energy, which may flip their spins in a random manner[19]. An interaction with the magnetic fields created by neighbouring particles also “steers” the carriers and thus requires no energy. This therefore generates rapid changes in spin polarization of carriers. If one observes the spin-polarization of the current at another position within the material, it will be considerably weaker than at the point of injection.

3.8 Spin-Orbit Interactions and the Rashba Effect

On page 15, the Lorenz force was described as the total force acting upon a moving charged particle in a magnetic field.

$$\mathbf{F} = q(\mathbf{E} + \mathbf{u} \times \mathbf{B})$$

If, however the particle has non-zero spin and is moving at a velocity close to the speed of light, an effect known as Spin-Orbit Interaction occurs. In this case, a static electric field perpendicular to the velocity of the particle produces a *magnetic* field effect on the particle. This interaction affects the spin-dynamics and energy of the particle and leads to the precession (or rotation) of spin. The effective magnetic field component due to spin-orbit interaction is given by:

$$\mathbf{B}_{\mathbf{eff}} = \frac{1}{c}(\mathbf{u} \times \mathbf{E})$$

The total magnetic field acting upon the particle is therefore the sum of the applied magnetic field and the effective magnetic field due to the spin-orbit interaction:

$$\mathbf{B} = \mathbf{B}_{\mathbf{app}} + \frac{1}{c}(\mathbf{u} \times \mathbf{E})$$

The Lorenz force acting on such a system may now be expressed as shown in Equation 7. A full derivation of this equation is given in Appendix II.

$$\mathbf{F} = q\left(\left(1 - \frac{u^2}{c}\right)\mathbf{E} + \mathbf{u} \times \mathbf{B}_{\mathbf{app}} + \left(\frac{\mathbf{u} \cdot \mathbf{E}}{c}\right)\mathbf{u}\right)$$

Equation 7: Lorenz Force Incorporating Spin-Orbit Interaction

The Rashba Interaction[20] is a specific form of Spin-Orbit Interaction. It leads to spin-precession in systems in which a planar flow of charged particles, travelling in one-dimension is subjected to an electric field normal to the plane (Figure 4). In Spintronics, this is an extremely important effect as it allows spin polarization to be rotated by the application of a gate voltage to a device. Consequently, devices such as the Spin Transport Field-Effect Transistor have been conceived.

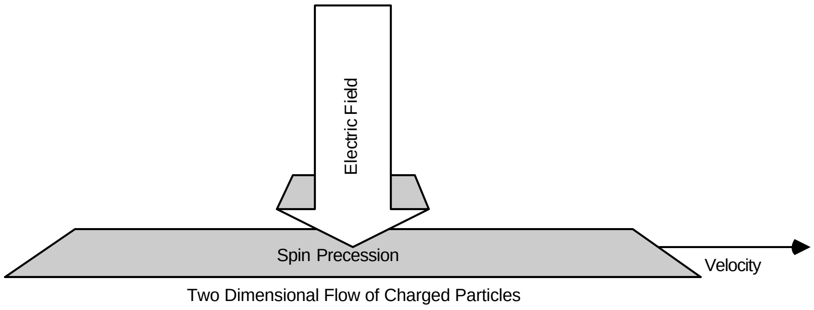

Figure 4: Illustration of the Rashba Effect

3.9 Giant Magnetoresistance (GMR)

An important result of the spin splitting of energy bands in magnetic materials is that the resistance of the material varies depending on the spin-polarization of the current. This effect is known as anisotropic magnetoresistance (AMR). A non-polarized current may be regarded as the sum of two separate components (spin-up and spin-down), each subject to a different resistance in the ferromagnetic material (Figure 5).

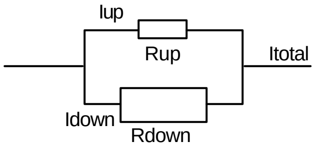

Figure 5: AMR in a ferromagnetic material

When two ferromagnetic materials are placed in series, separated by a non-magnetic conductor the effect is much larger and is called Giant Magnetoresistance (GMR). The relative magnetizations of the two layers determine the total resistance of the structure. When both magnetizations are aligned, the effect is similar to that described for AMR. One polarization of the current will experience significantly higher resistance than the other (Figure 6).

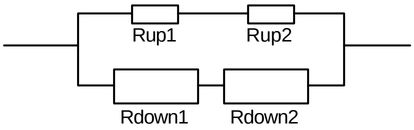

Figure 6: GMR effect for aligned ferromagnetic layers

However, when the two layers have antialigned magnetizations both current polarizations experience a large resistance (Figure 7).

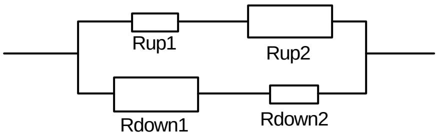

Figure 7: GMR effect for antialigned ferromagnetic layers

Consequently, the total impedance of the structure varies with the magnetization of the ferromagnetic layers.

A similar effect exists in tunnelling devices, known as tunnelling magnetoresistance (TMR), where the tunnelling current decreases as the ferromagnetic layers are antialigned.

4 Spintronic Device Structures

4.1 The Spin Valve

This is a fundamental device in Spintronics. A thin conductor is sandwiched between two layers of ferromagnetic material[21]. The Current Perpendicular to Plane (CPP) spin-valve (Figure 8) passes current through all three layers from top to bottom. The magnetization of the top layer of ferromagnetic material is fixed i.e. its variation with respect to external magnetic fields is small. This may be achieved in a number of ways including the addition of an anti-ferromagnetic top layer to form an extremely stable magnetic field loop or the exploitation of magnetic anisotropy.

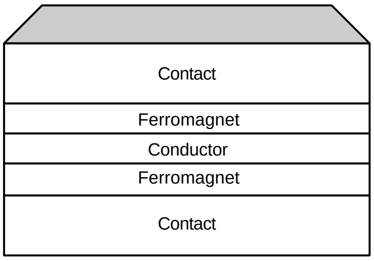

Figure 8: Vertical CPP Spin-Valve

The spin-valve is a practical device, which exploits the GMR effect. When the magnetization vectors of the two magnetic layers are aligned, the resistance of the device is minimised. Conversely, when the magnetization vectors are anti-aligned, the resistance is maximised. A figure of merit for the spin-valve is the magnetoresistance ratio[22], defined in Equation 8. This is the decrease in resistance as the magnetization vectors of the ferromagnetic layers move from antialigned to aligned, relative to the resistance in the aligned state. Magnetoresistance ratios of around 25% are achievable and allow the device to be useful in practical terms[23].

$$\text{Magnetoresistance Ratio} = \frac{R_{\text{Antialigned}} - R_{\text{Aligned}}}{R_{\text{Aligned}}}$$
$$= \frac{\Delta R}{R_0}$$

Equation 8: Magnetoresistance Ratio for Spin-Valve

A variation is the Current-In-Plane (CIP) spin-valve (Figure 9), which passes current through the device from left to right[24]. In this case, a complex reflection pattern occurs when the magnetization vectors are anti-aligned, leading to high resistance in the channel. The CPP geometry is generally preferred as it yields higher magnetoresistance ratios.

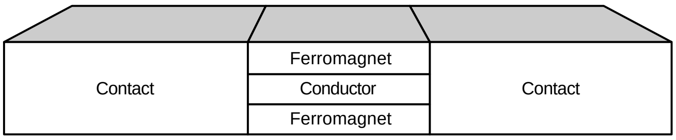

Figure 9: CIP Spin Valve

4.1.1 The GMR Read Head

The all-metal spin-valve has already shown its worth in computer applications in the form of the GMR read head[25,26]. For many years, read-heads in magnetic media devices such as the hard drive were made from tiny wire coils in which a current would be induced as it passed over magnetic domains in the media. The direction of magnetization of domains would correspond to the direction of the induced current. The bulky inductive read head however became the limiting factor in the density of the media.

The GMR read head is effectively a spin-valve with its free ferromagnetic layer parallel to the magnetic media[27]. Rather than inducing a current in the read head, the resistance of the read-head is modulated. As spin-valves may be made with extremely small dimensions, the density of magnetic domains on hard disks has increased dramatically. Spintronics has therefore led to a vast improvement in the capacity of magnetic media and hence the cost of bulk data storage.

4.2 The Magnetic Tunnel Junction (MTJ)

A similar device to the spin-valve is the magnetic tunnel junction. In this case, tunnelling magnetoresistance (TMR) effects are exploited by using an insulating layer rather than a conductive layer for the channel. Conduction is therefore achieved by quantum tunnelling rather than ballistic transport. As in the case of the spin-valve, the MTJ exhibits a change in resistance depending on the applied magnetic field.

4.3 Magnetoresistive Random Access Memory (MRAM)

Random access memory (RAM) forms the primary storage in modern computer systems. Several types of RAM exist, each having several key advantages and disadvantages. In general, however RAM is expensive at around 150 times the price per megabyte compared with a typical hard disk. Hard-drives are used as bulk storage due to their non-volatility and high storage density.

Static RAM (SRAM) is extremely fast, storing bits as latched logic states between two logical invertors. The latched states are extremely stable and last for long periods provided a power supply is maintained. Each bit of information requires six MOSFETs, so SRAM is dimensionally large and expensive. It is therefore used mainly as core data storage i.e. in registers in processors and other small, high-speed caches.

Dynamic RAM is very compact, as only a single transistor and capacitor pair is required for each bit of data stored. The transistor is used to control access to the storage element (the capacitor). As the capacitor is small, the leakage current causes significant decay in the stored voltage. Thus, each bit must be refreshed every few microseconds. In addition, reading the voltage requires the capacitor to be drained. This refresh cycle, combined with the charging and discharging times makes the DRAM much slower than SRAM. The higher integration however makes it much cheaper and therefore, DRAM is used as the main block of primary storage.

A third general type of semiconductor memory is rewriteable Read Only Memory (ROM) such as Flash-ROM. These devices have an advantage in that they are permanent data stores, which allow their contents to be updated electronically. Write-cycles are normally slow, and they are expensive but read cycles are comparable to other forms of semiconductor ROM. Typically, Flash-ROM is used to store Basic Input Output System (BIOS) settings, which are small and are required at high speed, but may require occasional updates.

MRAM however may provide all of these advantages in a single device. The capacitor in a DRAM bit is replaced by a spin-valve or MTJ. Data is stored by applying a relatively large magnetic field to the spin-valve, thus magnetizing its free layer in a particular direction. The data is then read by passing a small current through the spin-valve. The size of the resistance indicates the logic level stored. As the magnetization of the spin-valve is a quick process, MRAM has approximately the same speed as SRAM whilst having similar density to DRAM (and eventually similarly low cost). In addition, as the magnetization of the spin-valves is stable, MRAM shares the non-volatility of Flash-ROM but with superior write times.

A unique advantage of MRAM is that no semiconductors are used. This means that MRAM is intrinsically radiation hard. As curie temperatures of over 1000K are typical for ferromagnetic metals, the operating temperature range of MRAM will be very large[28]. These two factors make MRAM an ideal choice for use in high-radiation or high-temperature applications. For military applications, the development of MRAM will be an obvious advantage.

Much progress has been made in the development of MRAM in recent years. The typical architecture at present is essentially a modification of the ferrite RAM (FRAM) used in the 1960's, with an array of MTJ storage elements replacing the coils found in FRAM. As a result, the design process has been facilitated somewhat. As MTJs are now available with a magnetoresistance ratio of over 50%, MRAM is also practically realisable. In 2003, a 4MBit MRAM chip was demonstrated by Motorola[29], which implies that very soon MRAM will be available with sufficient size and low enough cost to form core memory in computer systems.

One of the main technological challenges remaining is the efficient switching of magnetization in MTJs. Currently, MRAM relies on the application of a current parallel to the storage element to generate a magnetic field. This process however has a very low efficiency of around 1×10^{-6}. Experimental results suggest that a current as large as 10mA is required to switch the magnetization.

Other challenges include the improvement of fabrication tolerances and down size scalability.

4.4 The Spin Transport Field-Effect Transistor (Spin-FET)

One of the most important predictions of Spintronics from a commercial point-of-view is the Spin-FET. This device was proposed by Datta and Das in 1990 as an electronic analogue of the electro-optic modulator[30]. The structure is similar to that of the High Electron Mobility Transistor (HEMT), but with ferromagnetic contacts (Figure 10).

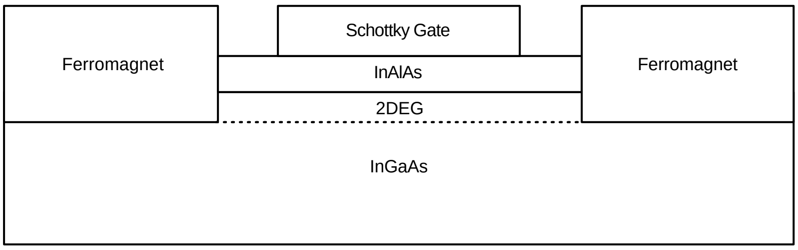

Figure 10: Structure of Spin-FET

This spin-FET has two means of controlling the flow of carriers through the device. Firstly, ignoring the effect of the gate voltage, the GMR effect may be used to vary the effective impedance between the drain and source contacts. Secondly, by applying a gate voltage, a strong electric field is placed perpendicular to a Two-Dimensional Electron Gas (2DEG) channel and the Rashba effect causes spin-precession. Thus, the gate voltage changes the spin-polarization of the current before it reaches the drain contact and either enhances or decreases the magnetoresistive effect.

At a trivial level, the spin-FET may be integrated into existing technology to replace standard FETs. Its main advantage however comes from its reconfigurable nature. Parallel current lines may be used during operation to apply a magnetic field to the spin-FET contacts and change the magnetization of one of the ferromagnetic contacts (c.f. the spin-valve). By doing this, the function of the transistor is changed – the effect of the gate voltage is inverted. Consequently, systems capable of reconfiguring at high speed during operation are made possible. This would allow efficient use of die-area in integrated circuits and much faster computation in digital systems. Many applications in the field of magnetic sensors are also feasible. An example of the possible use of spin-FETs in digital systems is given in section 6.2.

The fabrication of spin-FETs faces four main challenges[31]:

- Efficient injection of spin-polarized currents into a semiconductor
- Spin-transport through the channel material
- Effective control of the spin-system (e.g. by the Rashba Effect)
- Efficient detection of spin-polarized currents

4.5 The Hybrid Spin-Valve

The focus of the practical element of this project is the fabrication of hybrid spin-valve structures. The hybrid spin-valve is different from a conventional spin-valve, in that the channel for spin-conductivity is a semiconductor rather than a non-magnetic metal. Ultimately, it is envisaged that the hybrid spin-valve will form a substructure of the spin-FET (section 4.4), although many desirable characteristics as a device in its own right have been predicted. Firstly, the higher channel resistance would allow observable magnetoresistance for a shorter channel than that in an all-metal spin-valve. This would allow magnetic field sensors to be miniaturized further and hard-drive densities to increase. High magnetoconductance ratios (up to 90% for a 2DEG channel) have been predicted as a maximum, which would allow practical switching devices to be achieved[32]. For these reasons, the development of the hybrid spin-valve is an extremely important objective in the task of unifying magnetic storage media and active semiconductor devices.

5 Designing the Hybrid Spin-Valve

The practical aim of this project is therefore to design, fabricate and test a hybrid spin-valve. There are many proposed device structures. The main variables affecting spin-transport are the geometry of the channel, the channel material and its doping profile. The magnetic properties of the contacts are determined by their shape, material and growth methods.

5.1 Ferromagnet

Firstly, the design of the ferromagnetic pads will be considered. It is clear that the two pads must be substantially different in terms of their coercivity so that independent switching may be achieved. For optimal performance along a specific field direction, exploiting magnetic anisotropy may be a good solution. Such a device would contain one fixed pad with a high level of anisotropy and a free pad with low anisotropy. The anisotropic pad would switch magnetization at substantially higher field strength along its hard axis compared with the isotropic pad. The use of shape anisotropy has been suggested[32], although for the purposes of this project, a ready-made sample is available. Upon this sample, a cobalt layer has been grown epitaxially, and thus anisotropy is built-in to its crystal structure. This anisotropy is proven in section 7.6 using MOKE analysis. It has been suggested that interdigital ferromagnetic contacts would be useful for commercial devices as it acts like several devices in parallel and their magnetoresistive effects are averaged[42]. It is the author's opinion however that the space required for this geometry is somewhat larger than necessary. In practice, this may also lead to large numbers of rejected devices during fabrication as the probability of a short-circuit increases rapidly with the number of contacts in the device. Promising results have also been obtained by using shape anisotropy in a lateral device[33].

To enhance the anisotropic effects, a relatively thick layer of a very soft material should be used for the free contact. In this project, a 30nm layer of permalloy was chosen. Previous experiments show a switching field of around 20mT for permalloy contacts depending on their geometry, which should be sufficiently different from that of cobalt to allow independent switching[34]. Spin-polarization measurements of up to 20%, with a magnetoresistance ratio of up to 1% have been made for interfaces between ferromagnetic materials and semiconductors[35] although it has frequently been suggested that effects such as AMR or the Hall Effect may explain magnetoresistance ratios as low as this[36,37,38].

A number of suggestions have been made concerning the use of novel materials such as magnetic semiconductors or Heusler alloys[31,33,39,40]. These structures can theoretically inject a spin-polarisation of 100% into the channel with very low conductivity mismatch at low temperatures. Fabrication using such materials is however complex and beyond the scope of this project.

5.2 Semiconductor

The samples used in the practical work contained a highly p-type GaAs/AlGaAs quantum well. It has been suggested however that the use of a thin highly doped region of GaAs near the metal-semiconductor interface would reduce the schottky barrier height and therefore increase the level of tunnelling, improving the spin-injection[17]. An alternative approach is the use of an InGaAs/InAlAs or InAs/InAlAs quantum well, upon which most metals form an Ohmic contact. In this structure, a 2DEG acts as the channel, offering very high electron mobility and long spin-relaxation lengths. Theory predicts that in such a material, 100% spin polarization is possible[41], but in practice it appears that a maximum polarization of 4.5% is observed, which decays at temperatures above 10K and channel lengths above 450nm[42]. The polarization appears to decay by an order of magnitude as carriers pass through the Ohmic contact. Spin-coherence has however been demonstrated in GaAs, with a larger lifetime than in InAs, over 100ns[31]. A formula for the spin transport length in GaAs has been found in previous work at York[43], suggesting large values are possible (Equation 9).

$$l = \sqrt{\frac{kT\hbar E_g}{Aa^2 (k_B T)^3 m_e^*}}$$

Equation 9: Spin Transport Length in GaAs

As a result, this project focuses on the use of GaAs, for which a schottky contact exists with most metals.

5.3 Geometry

Due to the ease of fabrication and the superior magnetoresistance ratios achievable, the CPP design (section 4.1) was used in this project. Both vertical (Figure 11) and lateral (Figure 12) geometries have been used to fabricate the spin-valve in this configuration.

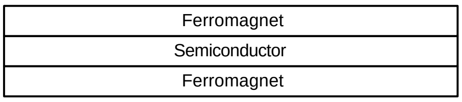

Figure 11: Vertical CPP hybrid spin-valve

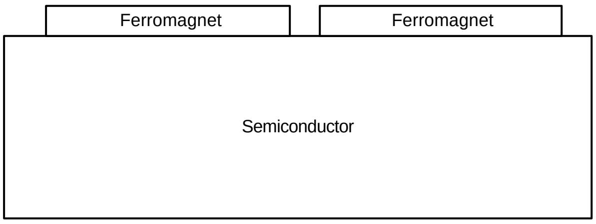

Figure 12: Lateral CPP hybrid spin-valve

The lateral device contains a nanoscale gap between the ferromagnetic contacts, with the channel existing in the semiconductor just beneath the gap. Clean interfaces can be achieved, but this geometry has poor definition of the channel length[33]. Furthermore, electron-beam lithography must be used to define the gap between the contacts and the actual dimensions are highly variable due to the proximity effect.

It is necessary that the channel length be less than the spin-relaxation length. For InAs, lengths of around 200nm have yielded success and reportedly, GaAs will have a larger spin-relaxation length still. The vertical device requires the definition of a nanoscale membrane between the two ferromagnetic contacts. A membrane thickness of around 500nm is readily achievable using selective etching. From Dr Ahmad's previous work on Ferromagnet/ Semiconductor structures, a 10mm x 20mm sample (number 080600) was available for use. Sample 080600 (Figure 13) consists of a 500µm thick GaAs substrate with the following epitaxially grown layers:

1) An etch-stop layer of $Al_{0.3}Ga_{0.7}As$
2) A second layer of GaAs in [100] orientation with high acceptor doping concentration

3) 15 monolayers of Co
4) 20 monolayers of Cr

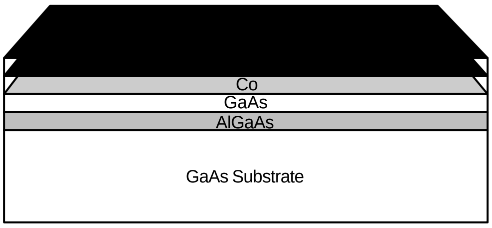

Figure 13: Sample 080600

The AlGaAs etch-stop layer allows an ammonium hydroxide (NH_4OH) based etching solution to leave a very thin layer with a smooth interface as AlGaAs has a negligible etch rate in NH_4OH compared with that of GaAs.

The GaAs layer acts as the channel for the spin-valve device and above this, the Co layer is used as the pinned ferromagnet. The Cr capping layer is used to protect the Co from degradation due to oxidation and other reactions. The capping layer is thin, so extra metal was deposited during device fabrication to allow for wire bonding and packaging.

The shape of sample 080600 is shown in Figure 14.

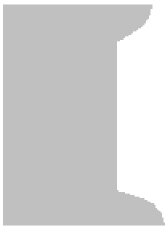

Figure 14: Shape of Sample 080600

This substrate used intrinsic GaAs as a substrate with a highly doped p-type material close to the metal-semiconductor interface to reduce the depletion width and the barrier height and increase the tunnelling current[17]. By using a 2DEG channel, much lower channel impedance would exist although the fabrication of such a device was beyond the scope of this project[33].

5.4 Pad geometry

It is shown in section 6.3 that the dimensions of the ferromagnetic pads will make a large difference to the loss resistance of the device as well as its resonant frequency. Therefore, in this project, the aim was to fabricate a number of devices with dimensions of 10µm and 100µm, using both circular and square masks and to confirm the effect on the device impedance.

By evaporating permalloy onto the GaAs, a high level of diffusion of metal into the semiconductor could be expected leading to significant surface states. Despite its disadvantages, this method was used throughout the project due to the ease of fabrication. For further work, it is suggested that MBE growth at around 10°C is used as a cleaner interface may be achieved[17]. A separate sample, C1773 was available, with the structure shown in Figure 15.

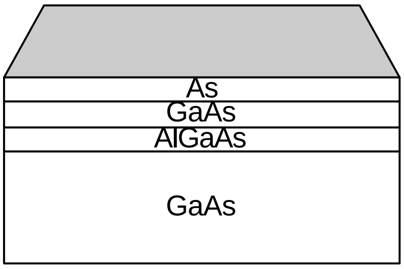

Figure 15: Structure of sample C1773

The structure is very similar to that of sample 080600, except there is no epitaxially grown ferromagnetic layer, and a thin capping layer of As (Figure 16).

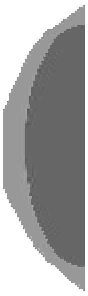

Figure 16: Shape of sample C1773

5.5 Fabrication Process

For sample 080600, the first step was to deposit additional capping metal over the metallic face. Following this, the back surface was etched down to around 100μm and a window of between 10μm and 100μm defined using photolithography. Selective etching was then used to remove the bulk GaAs and leave a thin AlGaAs/ GaAs membrane. Finally, permalloy and a capping layer were evaporated into the window.

For sample C1773, the same process was used with the exception of evaporation to prepare the sample for MBE growth. The plan for fabrication in future devices is to subject the sample to argon etching over the membrane to clean the surface before depositing a relatively thick layer of permalloy and a capping layer. The sample will then be rotated through 180^o and the As capping layer removed with further argon etching. Following this, a thinner layer of permalloy and a capping layer will be deposited on the surface to form the pinned ferromagnetic contact.

6 An Engineering Approach to Spintronic Devices

6.1 The Impact of Spintronics on Global Communications

The principle of hierarchical design is fundamental to Electronic Engineering. Take, for example, a simplified model of the Internet (Figure 17), which is composed of a vast number of separate networks joined together by bridges and routers. Each network contains several computers. Every computer is composed of a number of components: a processor, several storage devices and various input/output devices. In turn, these devices are made from substructures containing logic devices made from MOSFETs. It can therefore be seen that although the task of designing the Internet directly from fundamental components would be beyond human capabilities, the approach of designing from the bottom of the hierarchy upwards has created the vast and complex web around which modern society revolves.

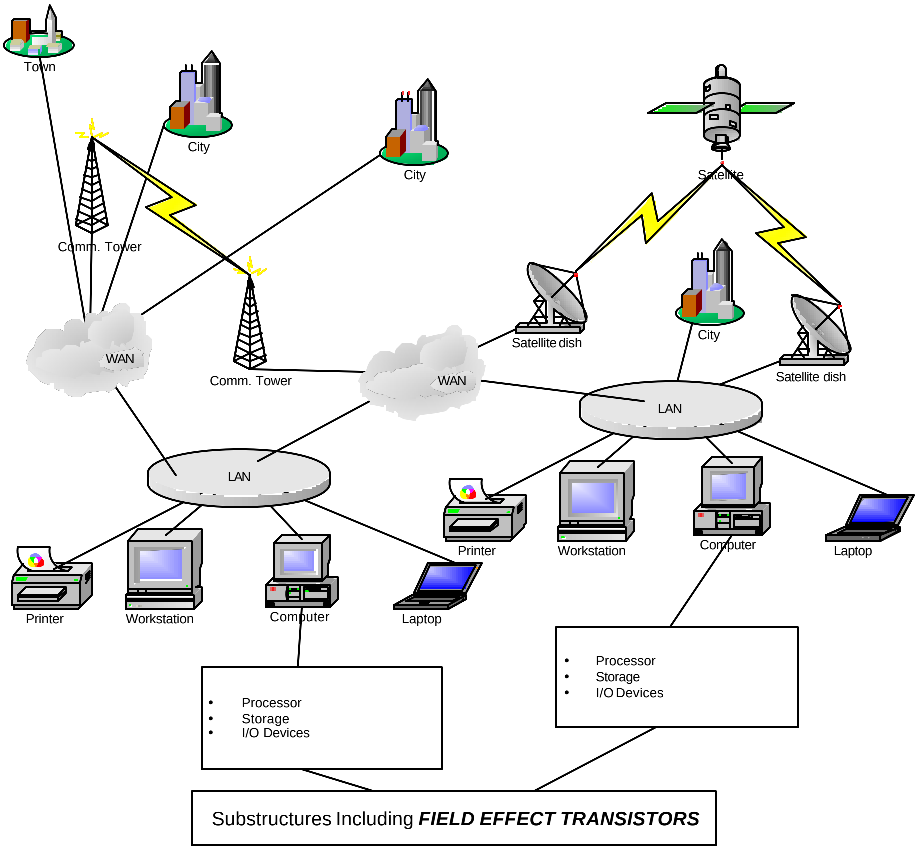

Figure 17: Simplified Structure of the Internet

From this view of Engineering Design, it can be seen that by changing any component in the system in general the effect will "ripple" upwards to the top of the hierarchy. Therefore by using a more versatile and efficient transistor (a fundamental component), *all* of the system has the potential to benefit.

When this theory is applied to the previous example of the Internet, one can envisage a future in which many computers take advantage of the benefits of Spintronics and are consequently faster, non-volatile and more adaptable. The Internet was created by the US Department of Defence, originally under the name "Advanced Research Projects Agency Network" or ARPANet, as a communications internetwork capable of withstanding a nuclear attack[44]. With this in mind, the non-volatility of MRAM would allow systems to be brought back on-line almost immediately if power grids were disrupted by an attack on a country's infrastructure. Thus, Spintronics has the potential to enhance communications and defence technology and move the Internet a large step forwards towards its ultimate goal.

Whilst this is a useful illustration of the benefits to society achievable through Spintronics, one may also note that FETs are ubiquitous in modern electronic systems and Spintronics may lead to significant advances in many areas of modern technology. In order to obtain the full advantage of Spin-FETs, we must again turn to hierarchical design principles and consider the impact on design of the next couple of levels above transistors in the hierarchy. Below, the potential impact on the design of digital systems is considered.

6.2 Programmable Logic Devices (PLD)

6.2.1 Logic Circuits

Digital systems rely on the operation of many interconnected logic gates. The most important types of logic gate are NAND and NOR type, from which all other gates may be constructed. Simpler in structure still is the logical inverter, or NOT gate, whose structure and functionality are shown in Figure 18 and Table 1 respectively.

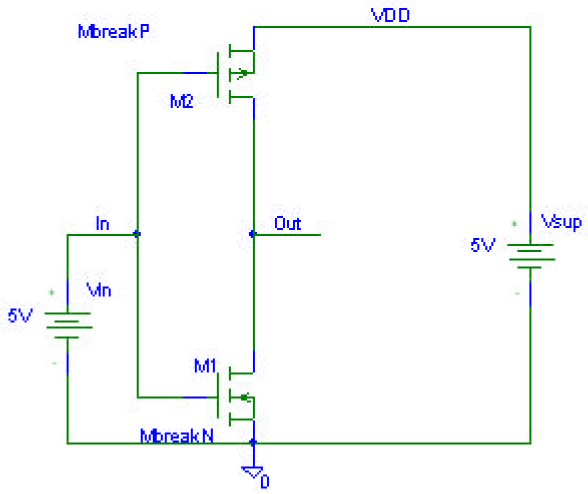

Figure 18: Internal Structure of the NOT gate

Vin	M1	M2	Vout
0V	OFF	ON	+5V
+5V	ON	OFF	0V

Table 1: Functional Behaviour of NOT Gate

The design shown above was entered into a PSPICE simulation, using the netlisting:

```
V_Vsup        Vdd 0   5V
V_Vin         In  0   5V
M_M1          Out In 0    0   MbreakN
M_M2          Out In Vdd Vdd MbreakP
```

The analysis command, “`.DC LIN V_Vin -2 7 0.1`” was used to simulate a linear sweep of input voltage from -2V to +7V.

The resulting output Voltage curve (Figure 19) shows a clear inversion of input voltage as expected.

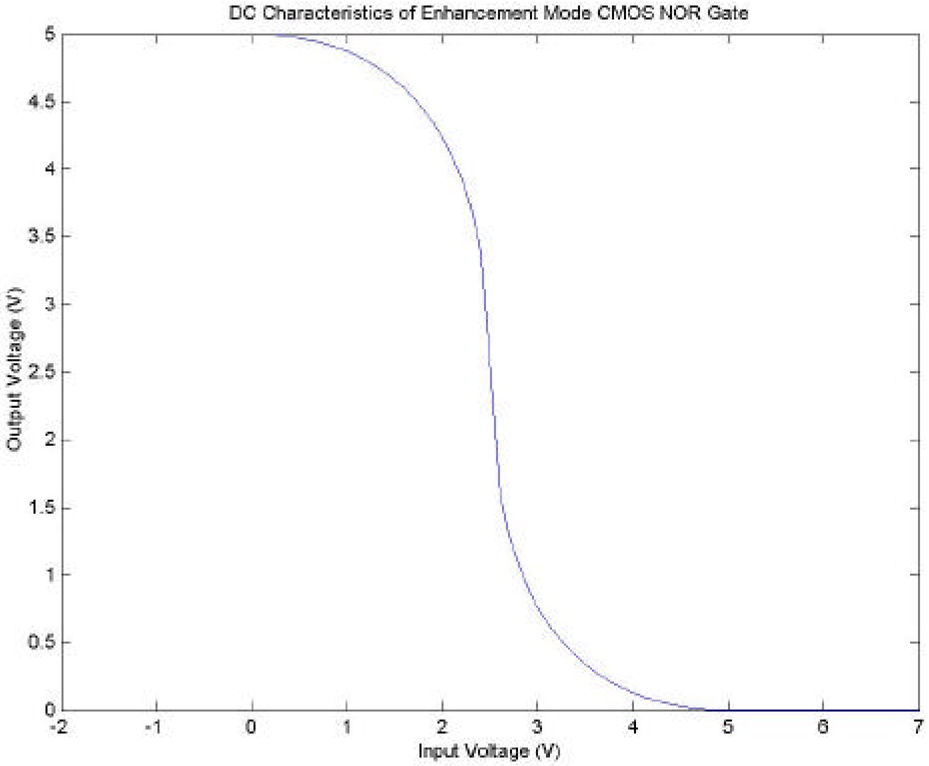

Figure 19: DC Characteristics of Enhancement Mode CMOS NOR Gate

By simply swapping the positions of the NMOS and PMOS transistors, the function of the device changes to a Source-Follower Buffer Amplifier[45]. In other words, the effect of the device upon the logic circuit is annulled. The DC transfer characteristics are shown in Figure 20.

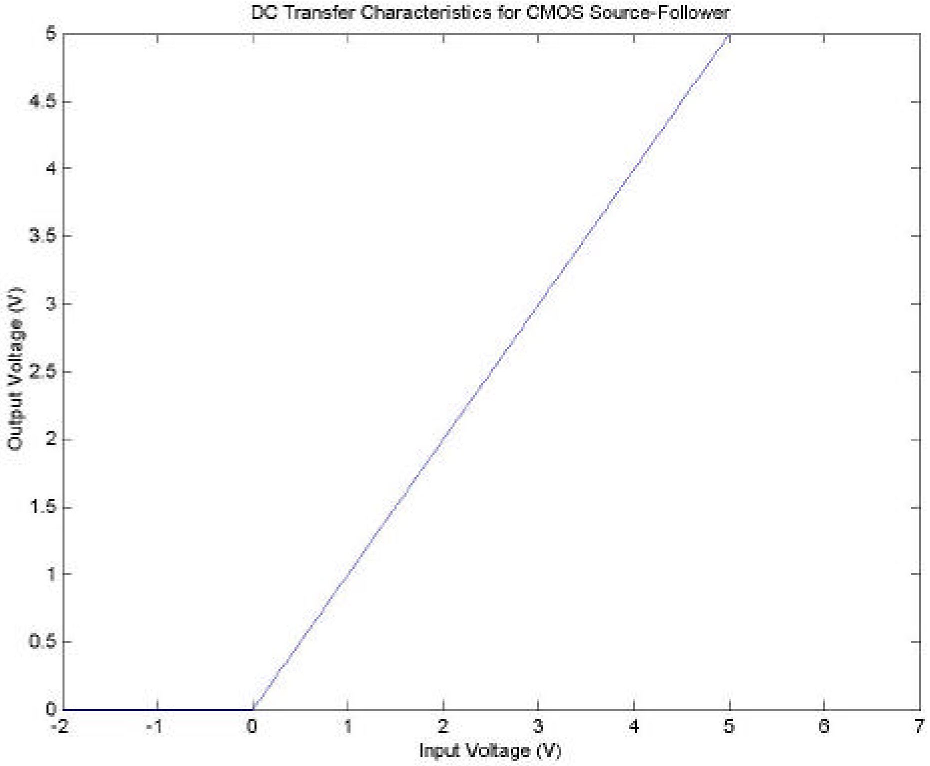

Figure 20: DC Transfer Characteristics for CMOS Source-Follower

By extending the analogy of the Spin-FET as an electronic counterpart to the optical polarization, we may consider a device consisting of a pair of optical waveguides running from a red and blue monochromatic light source respectively to a common output (Figure 21).

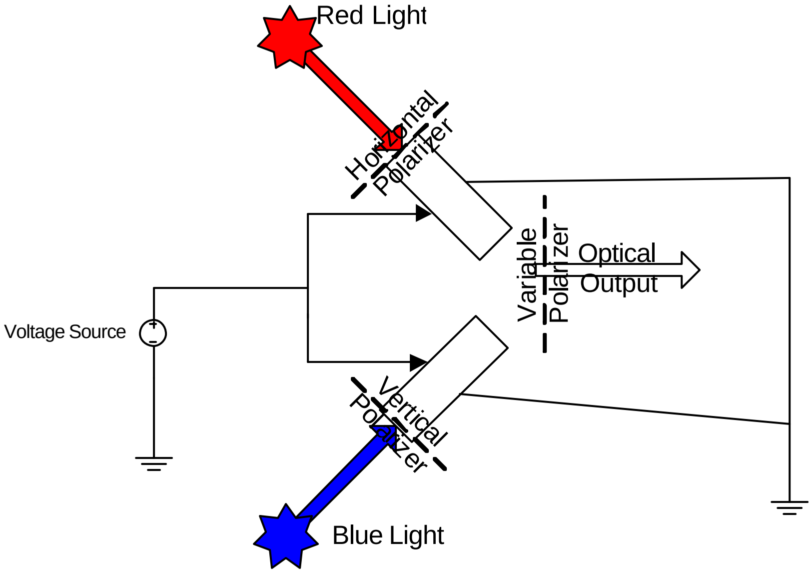

Figure 21: Voltage Controlled Dichromatic Light Source

By placing a fixed polarizer between each monochromatic light source and the optical waveguide to which it is coupled, the red light is horizontally polarized and the blue light is vertically polarized. A third polarizer at the output of the device may be rotated freely. The optical waveguides are fabricated from a material, which allows the polarisation of the photons to be rotated through 90^{o} by application of a voltage across the body of the waveguide.

Firstly, consider the output polarizer set in the horizontal position. When there is no input voltage, the red light passes through to the output whilst the blue light is blocked. Conversely, by applying a sufficiently high positive input voltage (say 5V); the red photons become vertically polarized and are therefore blocked whilst the blue photons become horizontally polarized and are therefore passed to the output.

The exact opposite effect occurs when the output polarizer is set in the vertical position. A summary of the device operation is shown in Table 2. It can be seen that by flipping the polarization of the output polarizer, the device's behaviour is inverted. It would be highly desirable to create a device capable of performing a similar task with an electrical output – i.e. a pass-or-invert logic device. A similar behaviour is exhibited by an exclusive-OR (XOR) gate whose symbol and truth table are shown in Figure 22 and Table 3 respectively.

Output Polarizer Orientation	**Input Voltage**	**Output Light Colour**
Horizontal	0V	Red
	5V	Blue
Vertical	0V	Blue
	5V	Red

Table 2: Behaviour of Voltage Controlled Dichromatic Light Source

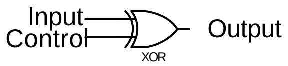

Figure 22: XOR pass-or-invert Logic Device

Control	Input	Output
0	0	0
0	1	1
1	0	1
1	1	0

Table 3: Truth Table for XOR Gate

Now, we may consider a device fabricated using a modified spin-FET like structure (Figure 23), where the application of a voltage across the substrate leads to rotation of the spin-polarization of carriers.

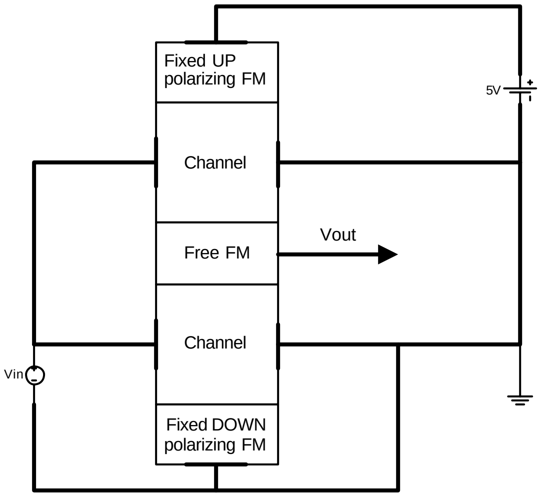

Figure 23: Spin-transport Pass-Or-Invert Device

The top ferromagnetic contact of the device is connected to the positive supply rail and is pinned to conduct only the UP polarized carriers. The bottom ferromagnetic contact is grounded and is pinned to conduct only the DOWN polarized carriers. The two channels are placed between contacts connected to the voltage input and ground. Consequently, a strong electric field is switched on or off by the presence or absence of an input voltage relative to ground.

If the central ferromagnetic contact is magnetized to pass only UP polarized carriers, then the top channel will conduct for zero input voltage whilst the bottom channel will act as a dielectric due to the GMR effect. The output will therefore be in electrical contact with the positive rail. Upon application of a 5V input, the electric field across the channels will rotate the spin polarization of the carriers through 180^o (assuming the device has been designed to meet this specification). The conductivity of the channels will therefore be the opposite of the previous case and the output will be in electrical contact with ground. The device will therefore act as a logical inverter.

Conversely, if the central ferromagnetic contact is magnetized to pass only DOWN polarized carriers then the exact opposite effect will occur. In other words, the output voltage will equal the input voltage. The device will therefore act as a logical buffer. Its behaviour is summarized in Table 4.

Magnetization of central contact	Input Voltage	Output Voltage
UP	0V	5V
	5V	0V
DOWN	0V	0V
	5V	5V

Table 4: Behaviour of spin-transport pass-or-invert device

We now have a device, which is capable of sensing changes in an external magnetic field. Furthermore, the output is in the digital domain and its connection to a digital device such as a microprocessor based control system will be trivial in its implementation and extremely fast as there is little requirement for additional interface hardware as would be required for a true analogue device. The output voltage may be used directly to indicate positive or negative field direction. Alternatively, the output voltage may be split into a parallel digital signal by an analogue to digital converter (ADC) to give higher precision.

As an example, one may consider such a device in a varying magnetic field. If the input is tied to 5V, the output will vary between 0V and 5V as the magnetic field direction changes. This signal may then be used as an analogue output, or by feeding it into a comparator, as a digital output representing field direction. In addition, by choosing to incorporate an ADC after the magnetic field detector, although there will be a penalty in terms of speed of operation the device can be connected to a parallel data port to provide a digital representation of field magnitude as well as direction (Figure 24).

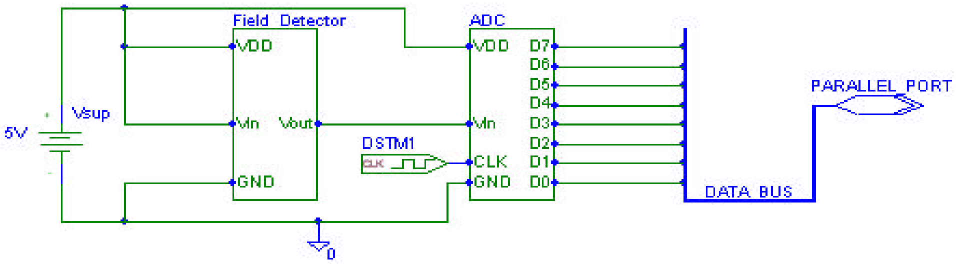

Figure 24: Magnetic Field Detector Including Interface to Microprocessor

6.3 Measurement of Spin Conductivity

It has frequently been suggested that the conductivity mismatch between a ferromagnetic metal and a semiconductor is a fundamental obstacle to spin injection[46]. The problem is twofold: firstly, interfacial imperfections lead to the formation of surface states, which promote carrier transitions within this region and reduces the spin injection. Secondly, the high impedance of the device dwarfs the magnetoresistance measurements.

In RF and Microwave engineering, however the matching of two systems with dissimilar impedances is a common (and readily solvable) task. By applying these principles, it is suggested that at a specific frequency the parasitic components of the device will resonate and minimize the bulk impedance. Thus, the magnetoresistive effect of the device will be more readily observable at the resonant frequency. This measurement will serve to validate the theory that conductivity mismatch is responsible for poor observation of magnetoresistance.

In order to minimise the impedance of the device, an equivalent circuit model must be found. Assuming the semiconductor has a low conductivity at room temperature; it may be considered as a lossy dielectric. If the ferromagnetic plates are considered to act as good conductors, then the overall structure of the device is that of a non-ideal parallel-plate capacitor (Figure 25).

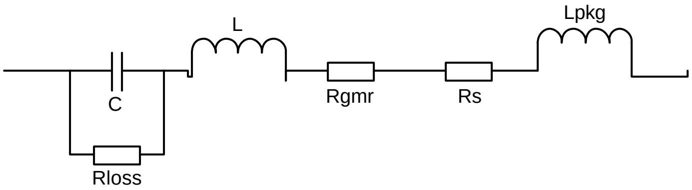

Figure 25: Equivalent Circuit Model for a Lossy Capacitor

The components in the diagram are described in Table 5.

Component Name	**Description**
C	The capacitance of the spin-valve structure, assuming it behaves as a parallel plate capacitor.
L	The inductance of the spin-valve structure, assuming it behaves as a parallel plate strip-line.
R_{loss}	The dielectric loss i.e. the bulk resistance of the channel material
R_s	Series resistance i.e. the loss in the metallic layers and in the packaging
L_{pkg}	Inductance in the packaging (around 2nH/mm of bond wire)
R_{gmr}	Magnetoresistive effects

Table 5: Description of Components in Equivalent Circuit Model

If the geometry of the device is as shown in Figure 26, then the similarity to a parallel-plate capacitor is clear. The thickness of the semiconductor is h, and the length and width of the plates are l and w, respectively. It is assumed that the bottom of the device is in intimate contact with a ground plane, whilst the top contact is connected to an output terminal via a bonding wire of length, r.

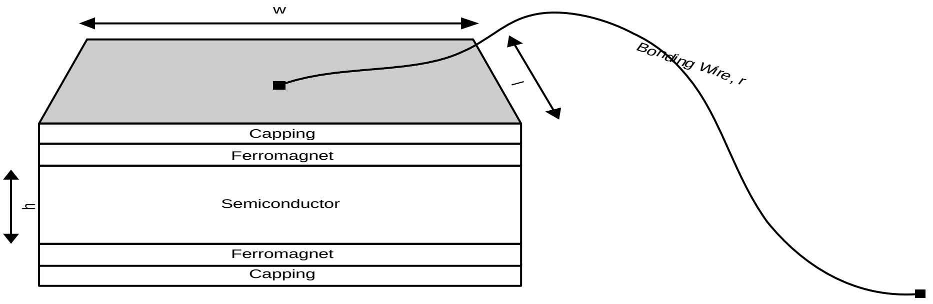

Figure 26: Device Geometry

The device has a capacitance defined by its dimensions given by the formula for a parallel plate capacitor as in Equation 10, where e_0 is the electrical permittivity of free space, e_r is the relative permittivity of the semiconductor, A is the area of the ferromagnetic plates and h is the thickness of the semiconductor.

$$C = \frac{e_0 e_r A}{h}$$

Equation 10: Capacitance of a Parallel Plate Capacitor

For a rectangular device, this expression reduces to $C = \frac{e_0 e_r lw}{h}$ and for a square device, to $C = \frac{e_0 e_r w^2}{h}$.

If the device is treated as a section of a parallel stripline, the inductance per unit length is given by Equation 11[9], where μ_0 is the magnetic permeability of free space and μ_r is the relative permeability of the semiconductor.

$$L' = \frac{m_0 m_r h}{w}$$

Equation 11: Inductance per Unit Length of Parallel Plate Stripline

For a standard (non-magnetic) semiconductor, μ_r is zero and hence the expression for the total inductance is $L = \frac{m_0 hl}{w}$, which simplifies to $L = m_0 h$ for a device with a square metal plate.

The loss resistance is the reciprocal of the conductivity of the semiconductor. The expression for conductance per unit length is given in Equation 12, where s is the conductivity of the semiconductor.

$$G' = \frac{sw}{h}$$

Equation 12: Conductivity per unit length for Parallel Plate Stripline[9]

For a square faced device, the total conductance is $G = \frac{sw^2}{h}$ and therefore the loss resistance is given by $R_{loss} = \frac{h}{sw^2}$.

The series resistance is given by the sum of the resistances of the two metal plates and the packaging. The contribution of the packaging to the total resistance will be strongly dependent upon small variations in fabrication methods and hence it is not possible to make an accurate prediction. This resistance component is therefore omitted from the following calculations. As this resistance does not affect energy storage within the device, it is assumed that the calculation of resonant frequency will remain accurate. In order to observe the GMR effect most clearly however, the resistance of the packaging should be minimised by using small, clean bonds wherever possible.

The impedances of the components may now be written as in Equation 13, where $\mu_{top,\ bottom}$ and $s_{top,\ bottom}$ represent the magnetic permeability and conductivity of the top and bottom contacts and f is the frequency of the transmitted voltage wave.

$$R_s = \sqrt{pf}\left(\sqrt{\frac{m_{top}}{s_{top}}} + \sqrt{\frac{m_{bottom}}{s_{bottom}}}\right)$$

Equation 13: Total Series Resistance of Device

Finally, the parasitic inductance of the bonding leads may be assumed to be approximately 2nH/mm[47], which will in fact dominate the inductance of the complete device.

We now have an expression for the impedance of each component in Figure 25 and circuit analysis may be used to find the resonant peak.

6.3.1 Example Calculation for Hybrid Spin-Valve

In order to make a useful prediction of device characteristics for a hybrid spin-valve such as that fabricated in this project, some values are assumed for the geometry.

- The channel is intrinsic (or lightly doped) GaAs, approximately 500 nm thick. In reality, a p-type material was used in this project although as the exact doping profile was unknown a worst-case model of its conductivity is used in this simulation.
- Both ferromagnetic pads are of negligible thickness in comparison with the channel and are 10µm squares.
- The top pad is made of epitaxially grown cobalt as in sample 080600, and the bottom pad is approximately isotropic iron. For simplicity, it is assumed that the relative permeability of the cobalt and iron are 250 and 4000 respectively and that both have a conductivity of around 10^7S/m.

Firstly, the capacitance is calculated using the expression, $C = \frac{e_0 e_r w^2}{h}$. For the device geometry used, w = 10µm and h=0.5µm. The permittivity of free space is 8.854 x 10^{-12} F/m and the relative permittivity of GaAs is 13.2. This yields a capacitance of 23.375fF.

Similarly, the device inductance may be calculated as 4p x 10^{-7} x 0.5 x 10^{-6} = 628.32fH. It may be assumed that good quality wire bonds of 2mm length are used, yielding a packaging inductance of 4nH. The total inductance is therefore around 4nH.

The conductivity of GaAs is determined from the carrier mobilities and the intrinsic carrier concentration at 300K. The hole mobility is 400cm^2/Vs, the electron mobility is 8500cm^2/Vs and the intrinsic carrier concentration at 300K is 2 x 10^6cm^{-3}. Using the equation $s = q(\mu_n + \mu_p)n_i$, this yields a conductivity of

284.8nS/m. The loss resistance is now calculated as $R_{loss} = 0.5 \times 10^{-6} / (284.8 \times 10^{-9} \times 10 \times 10^{-6} \times 10 \times 10^{-6})$ = 17.6GO. For doped GaAs, higher temperatures or shorter or wider channels, the loss resistance would be much lower.

The series resistance is calculated by substituting the values for iron and cobalt in Equation 13 as 6.373O, which is the approximate impedance of the device at resonance.

The resonant frequency is calculated using Equation 14 as 16.5GHz.

$$f_0 = \frac{1}{2p\sqrt{LC}}$$

Equation 14: Resonant Frequency of Device

In order to facilitate calculations for other device structures, a MATLAB simulation m-file was created, which is written in full in Appendix I.

The device model was simulated three times in PSPICE, incorporating a series magnetoresistance of 10O, 100O and 1000O respectively. A frequency response of the resistance is shown in Figure 27.

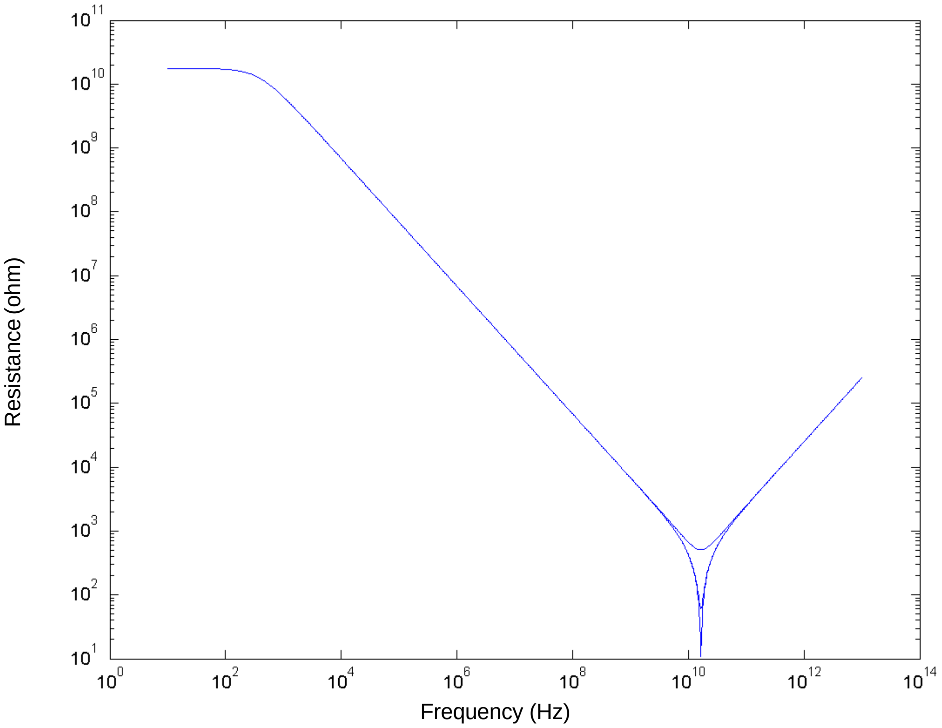

Figure 27: Resonance of Hybrid Spin-Valve Resistance

The simulation results clearly confirm that the GMR effect is most visible at the resonant frequency.

In order to perform these measurements in practice, it will be necessary to connect the device across the reflection port of a network analyzer. The analyzer must be set to measure the S_{11} (reflection coefficient) of the sample whilst the transmission port is unconnected. By applying a magnetic field along the hard axis of the pinned magnetic layer, a change in resistance at the resonant peak should be visible as the free layer switches magnetization. To confirm that it is the GMR effect causing the change in resistance as opposed to the Hall Effect, the measurements should be repeated along the easy axis of the pinned layer. Along this axis, the change in resistance should appear much lower as both layers will change magnetization at a similar applied magnetic field.

7 Preliminary Investigations

7.1 Introduction

The practical aspect of this project has aimed to achieve a number of goals as specified in the Initial Report[48]. Prior to commencing work on the fabrication of Spin-FET devices, it was essential to gain a good understanding of the practical techniques required. Health and Safety was considered and experimental apparatus was set up. Handling techniques were investigated. Following this, an extensive investigation was made into the etching processes to be used and a trial fabrication of the channel membrane performed.

7.2 Use of Glassware

Prior to experimental work, five 100ml glass beakers, a glass Petri dish and two glass 25ml measuring cylinders were purchased to avoid contamination of etching solutions. The glassware and the metal case in which they were stored were cleaned using Decon90 and allowed to soak for two hours before rinsing thoroughly with deionised water and wiped dry with new lint-free wipes then allowed to dry in air for several hours. The case was lined with lint-free wipes to adsorb any moisture from glassware after practical work.

The measuring cylinders were marked as follows:

1) “Slow Etch”: ammonium hydroxide or hydrogen peroxide.
2) “Fast Etch”: sulphuric acid, hydrogen peroxide or water.

It was particularly important to avoid measuring ammonium hydroxide (a base) or sulphuric acid in the wrong measuring cylinder to avoid neutralization and the formation of reaction products.

The Petri dish was used only for cleaning of the sample.

The beakers were marked as follows:

1) “Developer”
2) “Acetone”
3) “IPA”: Propan-2-ol

4) "Fast Etch": sulphuric acid, hydrogen peroxide or water.
5) "Slow Etch": ammonium hydroxide or hydrogen peroxide.

Again, it was important to avoid placing ammonium hydroxide and sulphuric acid in the wrong beakers; and to avoid mixing aqueous solutions and organic liquids to prevent precipitation of solutes.

All glassware was rinsed after use with either water (for the etching solutions) or with its intended contents for the rest.

7.3 Health and Safety and Handling Precautions

Prior to commencing experimental work, a risk assessment was carried-out and the appropriate COSHH forms studied. The following precautions were taken when handling substances:

- Waste acetone, photoresist and IPA were disposed of in an appropriate container whereas the etching solutions and developer were washed down the foul water drain with copious amounts of water.
- Sulphuric acid was added slowly to water when making etching solutions to prevent the acid from boiling and splashing.
- Similarly, sulphuric acid was rinsed away with slow running water far away from human contact.
- Whilst handling corrosive substances (hydrogen peroxide, sulphuric acid and ammonium hydroxide), a plastic apron, facemask and thick gloves were worn and the wet-bench shielding was kept in the lowest position possible.
- Bottles of corrosive substances, gloves, glassware and hands were washed after handling.

7.4 Substrate

A number of precautions are necessary when handling GaAs. Firstly, it is important to note that it is highly toxic and therefore contact with skin must not be allowed – gloves are to be worn during all practical work. Breathing the dust created when scribing or cracking GaAs is to be avoided. In particular, dust must never be blown away from the sample as this action creates a health and safety hazard and contaminates the clean working environment. To prevent contamination of water supplies, solid samples should not be allowed to fall into foul water drains. In one instance during this practical investigation, a specimen was accidentally dropped through the grating in the wet bench and it was necessary to stop the running water and recover it before water contamination could occur. In addition, it is important to note that GaAs is very fragile, and so work was required to establish good handling practices to avoid breakages.

7.5 Investigation into Etch Rates

As an initial step, the etching rate of GaAs was investigated. Two separate compositions of etching solution were used:

1) H_2SO_4:$3H_2O_2$:H_2O for the initial etching[49] as it etches both GaAs and AlGaAs quickly. This is a variation on the 1:8:1 solution used in fabricating the final device, as estimates already exist for etch rate[50,51,52].
2) $40H_2O_2$:NH_4OH for the final etching as it etches GaAs slowly, but does not significantly affect AlGaAs.

7.5.1 Sulphuric Acid Based Etch

7.5.1.1 Predictions

The INSPEC data for a 1:8:1 etching solution states that the etching rate at a temperature of 300K is 14µm/min, whereas Dr Ahmad's previous work in this area suggests an etch rate of between 3.5µm/min and 4µm/min. An etching rate of about 10µm/min therefore seemed realistic for a 1:3:1 solution. The clean room data states that this solution thins the GaAs substrate preferentially at high points implying that the resulting surface will be smooth.

7.5.1.2 Initial Testing

To establish a good handling procedure and to find an initial estimate of etching rate, the following steps were performed:

Sample Preparation

- A GaAs fragment, approximately 5mm x 5mm was immersed in RBS25 detergent for 30 seconds and then rinsed with deionised water. Very fine-tipped tweezers were used throughout this procedure and their tips were subjected to the same cleaning process as the sample.

- The sample was placed in a Petri dish with acetone and agitated for a further 30 seconds. The waste acetone was poured off into the waste bottle. This step was repeated.
- The sample was then placed in IPA for 30 seconds. The waste IPA was poured off into the waste bottle.
- To bake off any residual organic material, the sample was placed on a newly cut piece of aluminium foil on a hot plate at 150°C for ten minutes.

Photolithography

- A drop of positive photoresist was applied to the sample using a pipette such that half of the top surface was covered with a thick layer of photoresist whilst the remaining half was uncovered (Figure 28).

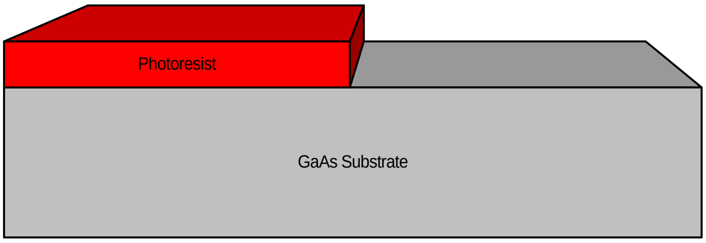

Figure 28: Photoresist Deposition on Test Sample

- The photoresist was baked for 10 minutes at 115°C.

Preparation of Etching Solution

- 5ml of deionised water was measured in a clean measuring cylinder and poured into the 100ml glass beaker marked “fast etch”.
- Wearing thick gloves, facemask and plastic apron, hydrogen peroxide was taken from the refrigerator and 15ml was measured in the same measuring cylinder and added to the water. The front screen of the wet-bench was kept as low as possible throughout this stage.
- The lid of the hydrogen peroxide bottle was replaced and the exterior of the bottle was rinsed well with water to prevent future users from coming into direct contact with any hydrogen peroxide spillage.

- The hydrogen peroxide bottle was returned to the refrigerator to minimise thermal decomposition according to the formula:

$$2H_2O_2(l)?\quad 2H_2O(l) + O_2(g)$$

- Whilst still wearing protective clothing, the sulphuric acid was removed from the acid storage drawer and a small quantity was dispensed into a beaker. The lid of the acid bottle was replaced, and the exterior of the bottle was rinsed thoroughly with water. The bottle was returned to the acid storage drawer.
- 5ml of sulphuric acid was measured in the measuring cylinder and added slowly to the etching solution to prevent the hydrogen peroxide from boiling, as the ionisation of sulphuric acid in water is highly exothermic.
- The unused acid was poured into the foul water drain with continuously running cold water. This was performed with the wet-bench screen at its lowest position, and the tap on the front of the wet-bench was turned at arms length. The measuring cylinder and beaker were rinsed five times with deionised water and allowed to dry.
- The heavy gloves and facemask were now removed to allow easy manipulation of equipment.

Etching and Removal of Photoresist

- The sample was placed in the etching solution for three minutes.
- After etching, the sample was immersed in deionised water to remove the etching solution. The water was changed three times during this process.
- The sample was immersed in three separate washes of acetone to remove the photoresist.

Measurements

- The sample was placed on the stage of the Alpha step measurement equipment with the highpoint to the left and the lowest point to the right.
- The needle was brought into contact with the highpoint of the sample at a distance of one needle-width from the step.

- The maximum range of 1000kÅ was selected and the needle height adjusted to be within the required band on the height gauge. The graphing pen was set to the zero position.
- The needle was moved through two automatic levelling phases and then moved across the step.
- A step height of 350kÅ (35µm) was measured, implying an etch rate of 11.7µm/min which matched the prediction well.
- Observation of the sample under an optical microscope showed a negative edge gradient when placed with the highpoint to the left. This is a desirable property, as deposited metal films will show a discontinuity over a positive edge gradient leading to problems with forming electrical contacts to the surface.

It was therefore decided that a 1:3:1 solution would be worth further investigation as an alternative etching solution.

7.5.1.3 Further Testing

To establish an etching rate, several pieces of GaAs were etched for varying lengths of time. In each case, the etch depth was measured using both optical microscopy and the Alpha step measurement equipment. To provide structural integrity and etching from the top surface only, the samples were mounted on glass slides using wax.

Sample Preparation

- Six squares were cut from a glass slide using a diamond tipped scriber.
- Six GaAs off cuts of around 5mm x 5mm were cleaned along with the glass squares and tweezers following the procedure described on page 54.
- The glass squares were transferred to a hotplate at 60^{o}C and using a scalpel, a number of pieces were scraped from a block of wax.
- A piece of wax, smaller than 1mm^3 was taken on a toothpick and placed on each glass square. After melting, the wax was distributed across the surface of each slide into an approximately even layer and the excess removed from the edges using a cotton bud.

- Each sample was placed onto the molten wax with the top surface upward, taking care not to contaminate the surface with wax. The samples were moved gently with tweezers to distribute the wax evenly underneath.
- The glass slides were removed from the hotplate and allowed to cool.

Photolithography

- A drop of positive photoresist was applied to each slide such that the slide was covered completely.
- Each slide was placed on the spinner and the resist was spun on at 4000rpm for 30 seconds.
- The photoresist was pre-baked for one minute at 115°C.
- A photo mask with a large black band was placed above each sample using the mask aligner so that half of each sample was covered by the mask and the other half was exposed (Figure 29).

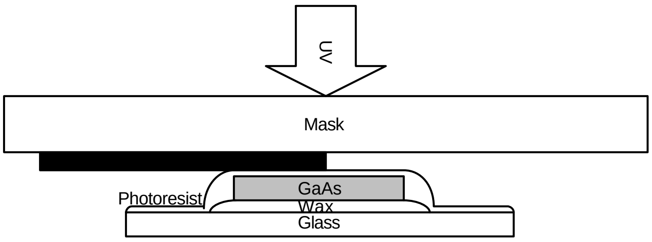

Figure 29: UV exposure of etch-test samples

- An exposure of 7 seconds at 300g contact force was used.
- The samples were individually placed in a beaker of positive resist developer for 45 seconds under constant agitation. They were removed, washed with deionised water and blown dry with nitrogen.
- Observation under the optical microscope showed that half of the sample was covered with photoresist and the other half was exposed as desired (Figure 30).

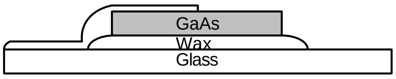

Figure 30: Etch-test samples following exposure to UV

Etching

- A 1:3:1 etching solution was prepared as described on page 55.
- All samples were placed simultaneously into the etching solution.
- At two-minute intervals, an individual sample was removed from the etching solution, rinsed with deionised water and blown dry with nitrogen.
- The etching solution was poured into the foul water drain with copious amounts of running water. The glassware was cleaned and allowed to dry before returning it to the storage container.
- Each slide was given a unique engraving using the scriber i.e. “2”,”4”,”6”,”8”,”10” or ”12” to represent the length of time for which each sample was etched.

Measurements

The step height for each sample was measured using the Alpha step measurement equipment as described on page 56. All samples, despite visually appearing to have different step heights yielded an Alpha step measurement of between 34µm and 36µm, thus indicating an upper limit of around 35µm for Alpha step measurements. It was therefore decided that all subsequent step measurements would be performed using optical microscopy. The initial measurements were therefore considered void.

The method used for these measurements was to focus the optical microscope on the lower level of the step and to note the number on the focussing wheel. The focus was then pulled upwards to the higher level of the step using the fine focussing wheel only. Initially, steps of 100 were used for coarse focussing and finally, small adjustments were made by moving the fine focussing wheel whilst continuously observing the sample. The difference in numbers read on the fine focussing wheel corresponds to the step height in microns.

Before performing these measurements, a test was performed by measuring the thickness of a set of metal feeler-gauge strips of known thickness. The known thickness was compared with the number of divisions through which the focussing wheel of the optical microscope was turned. The comparison is shown in Table 6, which confirms the scale of the focussing wheel to be 1µm/div.

Gauge Thickness (µm)	**Optical Measurement (divisions)**
100	102
150	158
300	284
400	416

Table 6: Confirmation of Optical Measurements

Each step was measured using the optical method described above and the results shown in Table 7.

Etching Time (minutes)	Etch Depth (µm)
2	34
4	52
6	58
8	74
10	84
12	100

Table 7: Etch Depth over Time for 1:3:1 Etching Solution

These values are displayed graphically in Figure 31 with a line of best fit. The gradient of this line was found to be 8.85µm/min, which appeared to match the original estimate of around 10µm well.

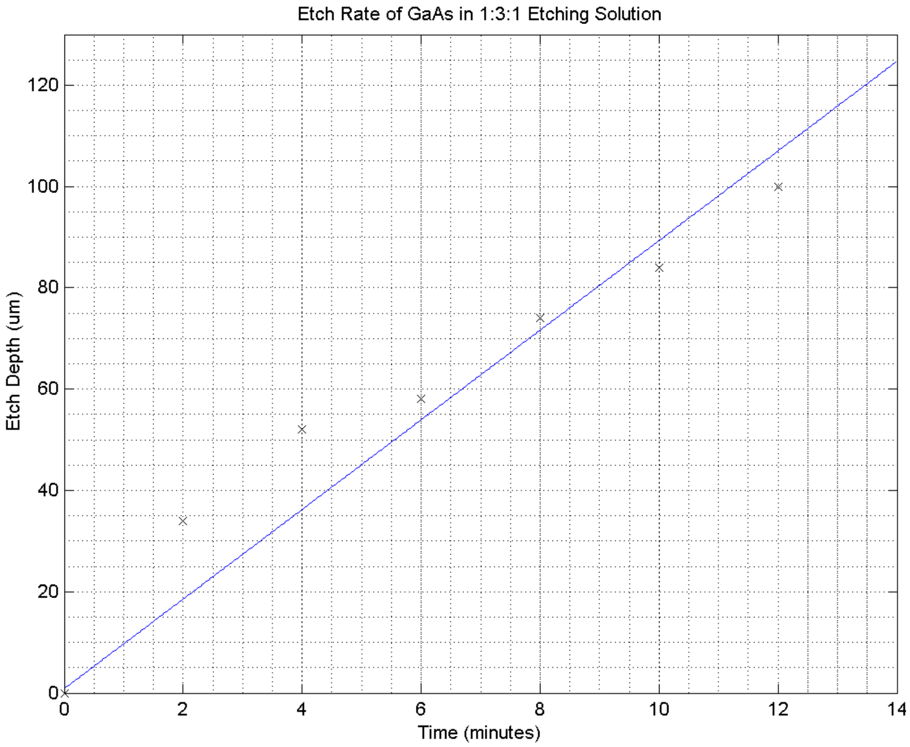

Figure 31: Etch Rate of GaAs in 1:3:1 Etching Solution

Several other observations were made:

- The wax rose above the edges of the sample and reduced the etching rate at these surfaces. The sample therefore exhibited a dip in the centre with respect to the edges.
- The wax melts at low temperature, whilst the dissolution of sulphuric acid in water is highly exothermic. Time must therefore be allowed for the etching solution to cool before attempting to etch a sample adhered to glass with wax.
- The wax is soluble in acetone and IPA and samples must not therefore be cleaned with either of these solutions whilst still attached with wax.
- The etched surface shows a regular pattern of short, shallow ridges. It was therefore decided that a thick capping layer of metal would be required to allow bonding to occur on top of the uneven surface.

7.5.2 Sample Handling Practice

As the available amount of GaAs, incorporating an etch-stop layer of AlGaAs was small, it was important to establish good handling techniques. The following work was undertaken to avoid wasting samples and experimental time during future work.

- A 5mm x 5mm GaAs off cut of around 500µm thickness was cleaned and a 1:3:1 etching solution prepared as described on page 54.
- The sample was immersed in the solution and allowed to etch until its thickness was around 100µm – the desired thickness of the spin-valve device. For this, it was assumed that an etch rate of 8.85µm/min would occur on both the top and bottom surfaces of the sample giving a total etch rate of 17.7µm/min. The time required to remove 400µm from the sample was therefore 400/17.7 ˜ 22min, 30sec.
- The sample was removed from the solution, cleaned in a beaker of acetone and then blown dry and transported to the hotplate.

The following observations were made concerning handling techniques:

- It was found that precision in handling the sample was aided by the use of fine pointed tweezers as opposed to flat-tipped tweezers.
- By resting the index finger on top of the two arms of the tweezers, greater control of pressure was possible. The arms were squeezed together between the thumb and middle finger.
- When removing the sample, the beaker was tilted to an angle of 45^o and gently agitated so that the sample would sit horizontally across the corner of the tilted beaker. The tweezers could then be gently inserted in the gap to aid lifting the sample.
- The beaker was placed on top of dust-free wipes to reduce the risk of dropping the sample down the drain when removing it from the solution.
- When blowing the sample dry, it was placed upon a dust free wipe against the shielding at the left hand side of the wet bench. It was held with tweezers in the left hand, at the right hand side of the wipe. The

nitrogen flow was applied from the right hand side of the sample, using the right hand. Therefore, if the sample were blown out from the grip of the tweezers, it would be stopped by the wet-bench shielding rather than falling down the drain.

- The sample appeared to by etched rapidly at its sides by the etching solution. It was therefore decided that the sample must be surrounded by a rim of photoresist during etching to prevent this from occurring.

7.5.3 Selective Etch Test

The selective etching solution of $40H_2O_2$:NH_4OH was to be used after the fast etching solution to etch through to the AlGaAs layer at which point the etching would slow to an almost negligible rate. It was still necessary to know an estimate of the etching rate so that the sample could be allowed to etch for sufficient time, avoiding the need to keep checking it at very regular intervals. In addition, it was useful in preventing the etching from being left so long that the AlGaAs layer was attacked.

7.5.3.1 Preparation

- A 5mm x 5mm GaAs off cut of around 500µm thickness was cleaned along with a small section of glass slide. A slight excess of wax was used so that the edges of the sample were protected from etching.
- The sample was stuck to the glass with wax and then etched in 1:3:1 etching solution until only 100µm remained. In this instance, as only the top surface was being etched, the approximate time for etching was calculated as 400/8.85 ˜ 45 minutes.
- The sample was removed from the wax by heating it to 115°C and sliding it off the glass.
- The glass and the sample were placed in a beaker of acetone until the bulk of the wax had flaked away or dissolved. Two further washes of acetone were used to clean away all visible traces of wax.
- The sample and the glass were transferred to a beaker of IPA for thorough cleaning and then blown dry in nitrogen and baked at 150°C for ten minutes to remove traces of organic contaminants.

- The sample was then stuck back onto the glass using a smaller amount of wax and allowed to set.

7.5.3.2 Photolithography

- The sample was covered with positive photoresist, which was spun on at 4000rpm for 30 seconds.
- The resist was soft-baked for one minute at 115°C.
- A small pinprick of approximately 200µm diameter was made in a clean sheet of aluminium foil for use as a positive mask.
- The sample was placed in the mask aligner, with the foil resting closely over its top surface and it was exposed to ultraviolet radiation for five seconds.
- The resist was developed for 45s and rinsed with deionised water before being blown dry.
- The resist was then hard-baked at 115°C for ten minutes.

7.5.3.3 Etching and Measurement

- Prior to etching, a measurement of the thickness of the photoresist was made using the optical microscope. This allowed the top of the photoresist to be used as a height reference throughout the experiment.
- Following the same safety precautions as in previous experiments, 20ml hydrogen peroxide were measured in the slow etch measuring cylinder and poured into the appropriate beaker.
- Using a graduated pipette, 0.5ml ammonium hydroxide was added to the beaker.
- The sample was placed in the etching solution.
- Throughout the etching process, bubbles of gas formed over the window on top of the sample. To remove the bubbles and allow the etching to continue, a stream of air from a pipette was used periodically to agitate the solution near to the window.
- At one-minute intervals, the sample was withdrawn from the etching solution and its step height was measured. The measurements are shown in Table 8.

Time (minutes)	Step Height (µm)	Etch Depth (µm)
0	2	0
1	4	2
2	6	4
3	8	6
4	10	8
5	12	10
6	15	13
7	19	17
8	21	19
9	24	22

Table 8: Etch Depth over time for Ammonia Based Solution

The values are shown graphically in Figure 32 along with a line of best fit. An etch rate of approximately 2.33µm/min was found from this line.

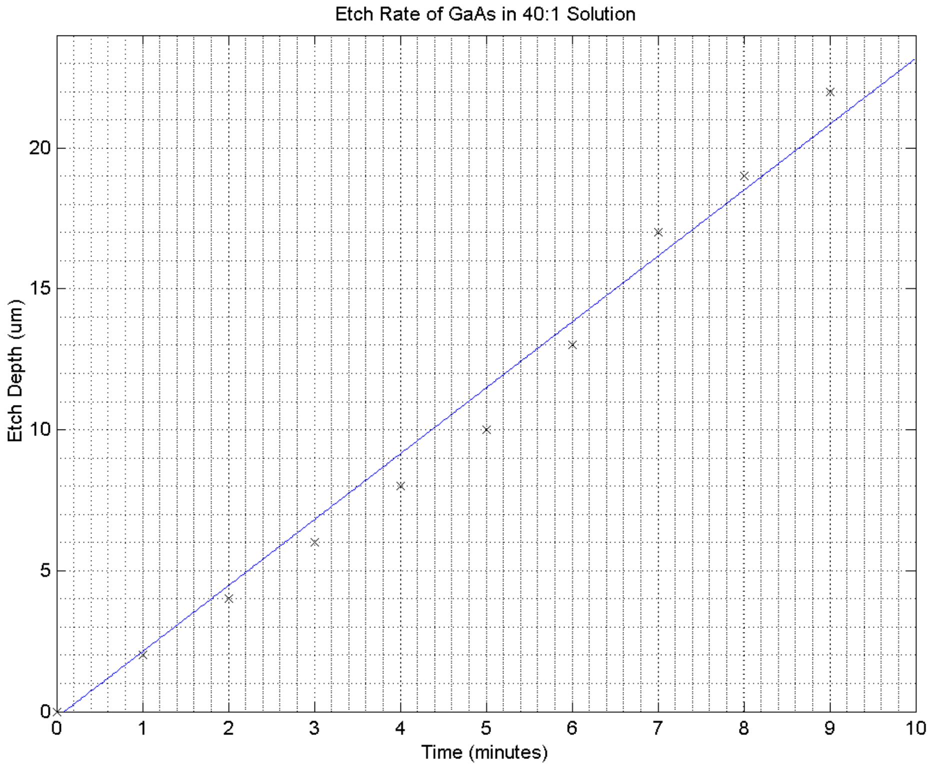

Figure 32: Etch Rate of GaAs in 40:1 Solution

7.5.4 Conclusions about Etching

Following the practical work described, it was decided that the etching would be carried out on the final device in a similar way to that used by Dr Ahmad in his previous work, with a few additional notes.

It was decided that a H_2O:8H_2O_2:H_2SO_4 solution would be used for the initial global etching and for the etching of the first 50μm of the window as in Dr Ahmad's work. As an alternative however, the H_2O:3H_2O_2:H_2SO_4 etching solution could be used for the initial global etching as it appears to exhibit a faster etching rate. To prevent etching of the sides of the sample when using the fast etching solution, an excess of wax was to be used in adhering the sample to the glass.

7.6 MOKE Measurements

In order for the final spin valve device to function optimally, a strong magnetic anisotropy in the existing ferromagnetic layer would be desirable. By aligning an applied magnetic field along the hard-axis of the device, the existing cobalt layer would remain relatively unaffected by a weak field whilst the magnetisation of an isotropic ferromagnetic layer would be changed considerably. Thus, the concept of a free and a pinned layer would be realized. MOKE measurements were therefore carried out on the sample to ensure its anisotropy was sufficiently large to allow a useful device to be fabricated.

7.6.1 Method

- Sample 080600 was cleaned following the method described on page 54 and attached to the sample holder of the MOKE equipment.
- It was aligned so that its long axis was along the 360^o direction.
- The sample holder was rotated so that the 360^o direction was perpendicular to the applied magnetic field i.e. the magnetic field was along the short axis of the sample.

- A number of trial runs were performed until a sufficiently large magnetic field was supplied to saturate the magnetization of the sample in both directions.
- Having established the required field strength, the discrete measurement points were specified by allowing five points to be measured in each saturation region and 20 in the region of changing magnetization. The desired density of points is shown in Figure 33.

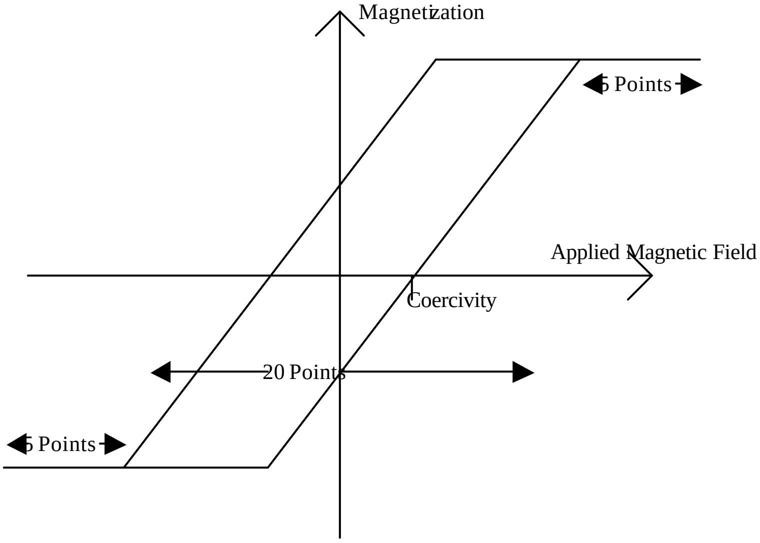

Figure 33: Density of Measurement Points for MOKE setup

- Having set up the measurement as described, five loops were swept and averaged and the data was saved as "`a360.dat`". The graph on screen was observed to ensure that it showed the expected shape of hysteresis loop.
- The sample was rotated through five degrees and the process was repeated. This was continued until the sample had been rotated through 180 degrees. In each case, the filename was chosen as "`axxx.dat`" where `xxx` corresponded to the angle of the sample from vertical in degrees.

7.6.2 Analysis of Data

The data files were stored as four columns of data as in the example of the first five lines of "`a270.dat`", which is shown below:

```
-0.06162    1.02816     0.09559     1.07190
-0.05677    1.02799     0.09075     1.07171
-0.05193    1.02802     0.08591     1.07182
-0.04709    1.02793     0.08107     1.07159
-0.04225    1.02791     0.07623     1.07164
```

Column 1 shows the magnetic field values on the up-sweep and column 2 shows the corresponding output MOKE voltages. Similarly, column 3 shows the magnetic field values on the down-sweep and column 4 shows the corresponding MOKE voltages.

These data were plotted as a hysteresis loop using a MATLAB function[53,54] stored in an m-file called "`moke.m`". This function is given in full in Appendix I.

The hysteresis loop for the sample at 270 degrees orientation (the easy axis) is shown in Figure 34. By way of comparison, the hysteresis loop for the sample at 360 degrees (the easy axis) using the raw MOKE data is shown in Figure 35.

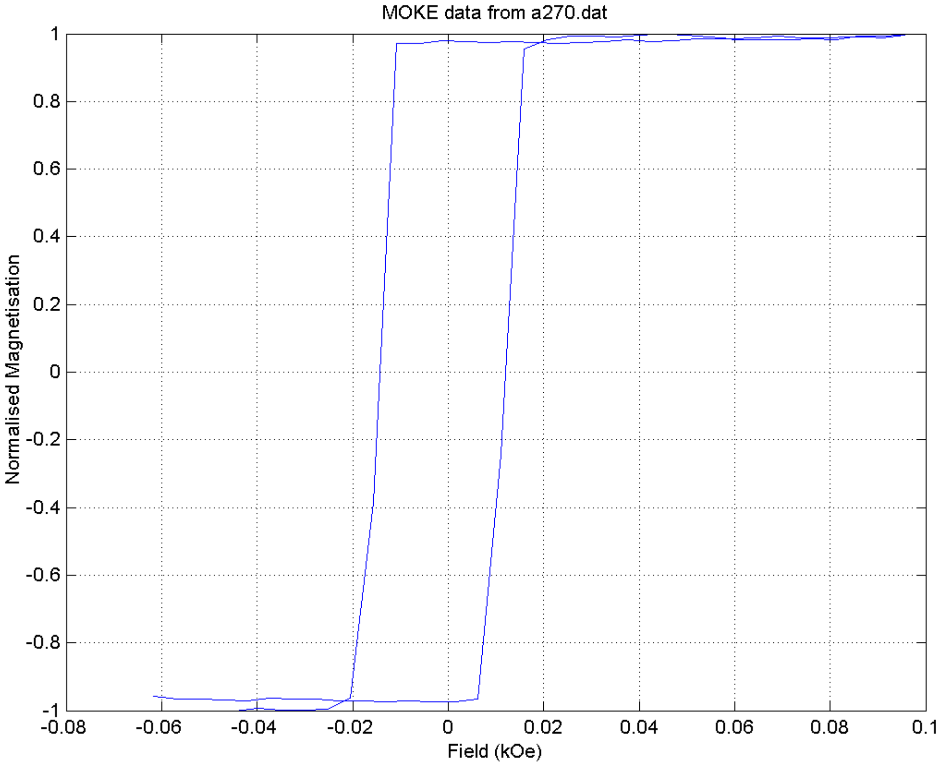

Figure 34: MOKE Data for 270 degrees orientation of sample (Easy Axis)

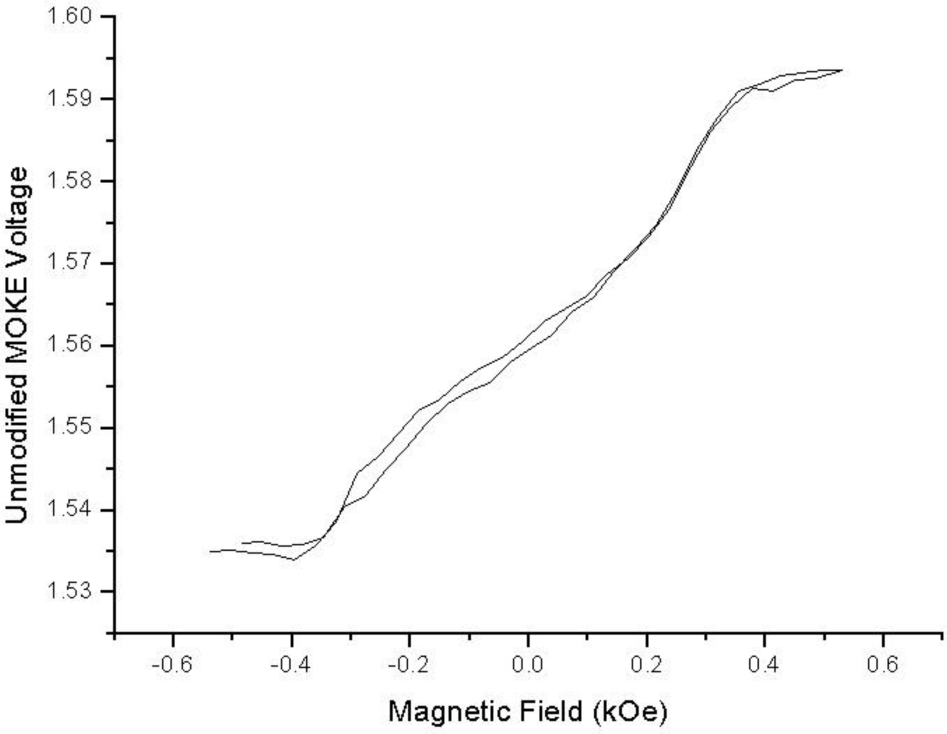

Figure 35: Unprocessed MOKE Data for 360 degrees orientation of sample (Hard Axis)

A second m-file was created to plot a graph of the variation of coercivity against field direction called "`graphcrc.m`". The graph generated for sample 080600 is shown in Figure 36. A very clear dip in coercivity is shown around 270° whereas the coercivity peaks at around 360° i.e. perpendicular to this. The hard and easy axes for the sample are shown in Figure 37.

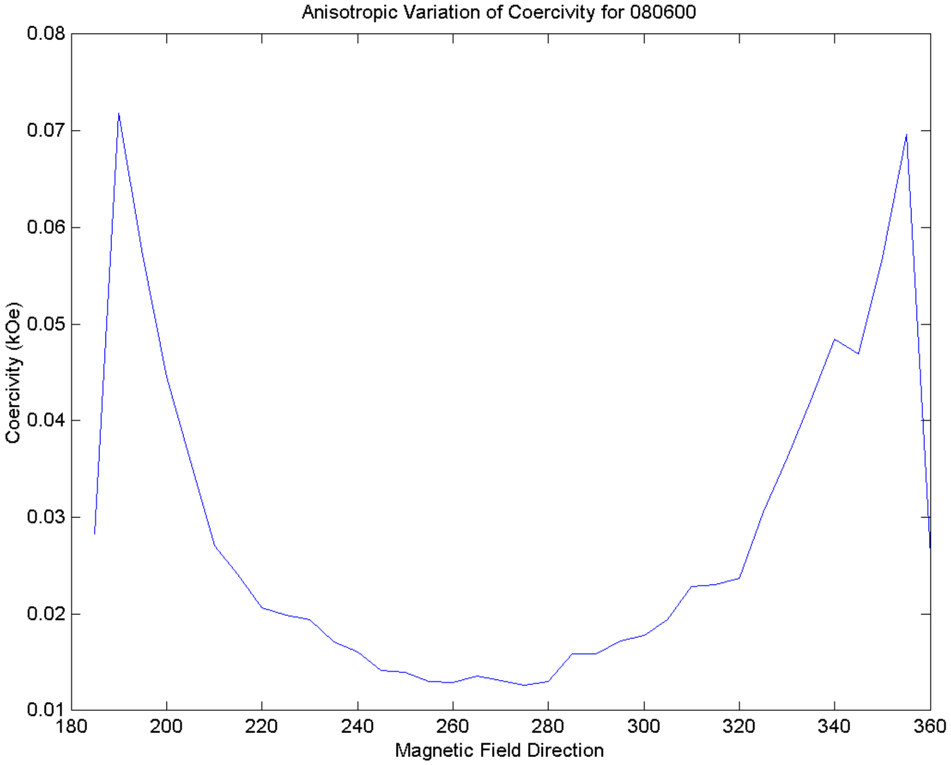

Figure 36: Anisotropic Variation of Coercivity for Sample 080600

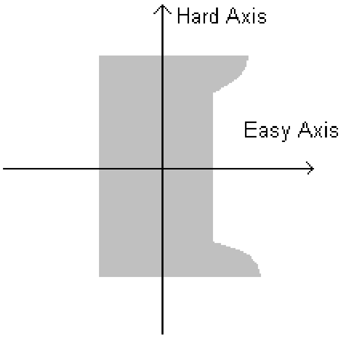

Figure 37: Axis Directions for Sample 080600

The sample in its current configuration therefore exhibits strong magnetic anisotropy. It was assumed that the anisotropy is a function of both the shape and crystalline structure of the material. Therefore, the effect of taking a square sample from 080600 would eliminate the shape anisotropy and rely entirely upon the component due to the crystalline structure. As the anisotropy is strong, it was assumed that even without the shape effect, sufficient anisotropy would remain to allow successful device operation.

7.7 Trial Fabrication of Membrane

As the formation of the very thin channel in the spin-valve is a critical step in its fabrication, work was carried out to investigate the practical techniques involved.

7.7.1 Sample Preparation

- Sample 080600 was held with a vacuum under the diamond tipped scriber.
- A dust mask, nitrile gloves and safety glasses were worn throughout the next steps to avoid inhaling highly toxic GaAs fragments.
- A pair of lines was scribed across sample 080600 to define the areas shown in Figure 38.

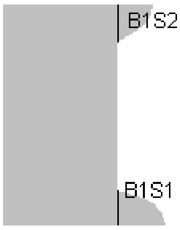

Figure 38: Batch 1 Samples from 080600

- Sample 080600 was cracked along the scribed lines using the edge of a glass slide for support. A dust-free wipe was placed over the top to minimise the release of GaAs dust.
- B1S2 was considered too small for fabrication to take place and was returned to the desiccator for safekeeping along with sample 080600.
- Sample B1S1 was cleaned and baked as previously described.
- B1S1 was mounted on a glass slide for protection using a small amount of photoresist with its metallic surface uppermost. Photoresist was used as the adhesive during this stage as wax would evaporate at low pressure

and potentially contaminate the sample or prevent the pressure in the evaporation chamber from reaching the required vacuum level.

7.7.2 Metallization of Top Surface

The aim of this stage was to deposit around 50nm of chromium and 300nm of gold, on the top surface of the sample to provide a good contact layer to protect the sample and ease packaging. A large hole was left for this trial, as it was desirable for the thin membrane to be visibly translucent with strong back lighting. This would allow a simple check of the etch depth relative to requirements.

- A blob of photoresist, around 1mm in diameter, was deposited on the metallic surface using a sharpened wooden stick (Figure 39).

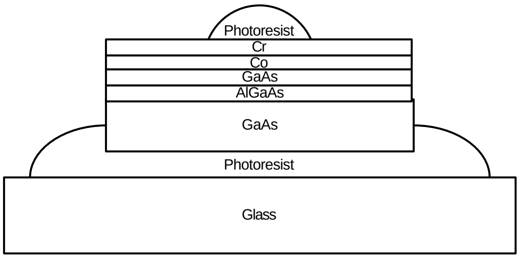

Figure 39: Deposition of Photoresist on B1S1 of 080600

- The two layers of photoresist were baked hard for ten minutes at 115°C.
- The sample was placed in the holder in the evaporation chamber, facing downwards towards the metal source.
- At the red supply terminal, several granules of chromium were placed in a previously used tungsten boat. The boat appeared to contain some contamination from gold but this was considered unimportant for the purposes of this trial.
- At the yellow supply terminal, a 2cm long piece of gold wire was cut into small lengths and placed in a new tungsten boat.
- Both boats were grounded via the blue terminal.
- The bell jar was replaced and the rotary pump was used to depressurize the chamber to 0.02torr.
- The rotary pump was then switched to backing the diffusion pump and the chamber was depressurized to 3×10^{-6} mbar.

- The deposition monitor was set with the required values for the materials used as shown in Table 9.

Material	Density	Acoustic Impedance
Gold	19.3	23.3
Chromium	7.2	28.94

Table 9: Material Properties for Evaporation

- The power supply was connected to the red terminal and the supply voltage gradually increased to 22V at which point the chromium began to glow.
- The shutter was opened and the deposition monitor activated.
- At a supply voltage of around 30V, evaporation commenced. After sufficient chromium was deposited, the shutter was closed. The deposition monitor displayed a thickness of 30.3nm as required.
- The chamber was allowed to depressurize to 3 x 10^{-6} mbar again and the monitor switched to the settings for gold.
- The gold melted around 28V and evaporation commenced at 35V. After 100nm had been deposited, the gold in the boat ran out.
- The contacts were allowed to cool and the chamber was vented.
- The tungsten boat containing chromium was removed and the boat containing gold was refilled with a similar quantity of gold wire.
- The chamber was depressurized again and a second evaporation of gold was performed. This time, the boat broke after 163nm had been deposited.
- It was decided that as around 290nm of metal had been deposited, it would be sufficient to allow easy packaging and to protect the sample.
- The photoresist was dissolved off in several washes of acetone.
- To verify the thickness of metal deposits, the Alpha step measurement equipment was used. The surprising result of 460nm was determined. As this height was too small to confirm with optical measurements, it was assumed that the thickness of the metal was at least 290nm and would be sufficient for the purposes of the trial.

7.7.3 Global Etching

In order to reduce the time required for etching, the entire substrate was etched down using a H_2O:$8H_2O_2$:H_2SO_4 etching solution to a thickness of approximately 200µm. This was chosen in preference to the 1:3:1 solution investigated previously as it yielded good results when used in previous work. It was decided that if etching was too slow, the faster 1:3:1 solution should be used in future attempts.

- The sample was stuck to a square cut from a glass slide using wax, with the metallic surface facing downwards.
- A 1:8:1 etching solution was prepared as in previous experiments and the sample was immersed in the liquid. It was assumed that the etching rate would be around 10µm/min and hence to remove a thickness of 300µm from the sample, 30 minutes of etching time was allowed.

7.7.4 Photolithography

A square window of around 200µm side length was to be defined on the GaAs face of the sample, surrounded by photoresist. This would allow etching to occur through the window only and thus create a small channel area for the device, leaving the bulk of the sample at a thickness of 200µm for structural strength. The initial method chosen was to align a negative mask over the sample and then to expose the photoresist through the corresponding positive mask.

- A pair of masks containing squares, circles and rectangles of varying dimensions was cleaned with water and IPA and then dried. The two masks were complementary i.e. each was a negative of the other.
- A 200µm x 200µm square near the centre of the negative mask was circled in red ink in order to highlight its position. The ink mark was made on the glass face of the mask to avoid damaging its delicate metallization. NB: On the negative mask, the square was opaque whereas on the positive mask, it was transparent.
- The corresponding square on the positive mask was isolated by covering all neighbouring squares with aluminium foil and electrician's tape.

When observed under the optical microscope, only the single square was transparent.

- Positive photoresist was spun onto the sample at 3000rpm for 40 seconds, and then baked on for a minute at 115°C.
- The sample was placed in the mask aligner and brought into contact with the negative mask at 800g contact force. This appeared to be too high a contact force as the sample was damaged in the process.
- The method of using prefabricated masks was abandoned at this stage, as it was not critical to forming a membrane in the sample. For subsequent stages, it was decided that a lower contact force would be used with the mask aligner.
- As a simple alternative, the foil mask described on page 64 was used for a five-second exposure.
- The photoresist was developed for 45s and examination under the optical microscope revealed a satisfactory window.

7.7.5 Etching

- A 40NH_4OH:H_2O etching solution was prepared. An etch-depth of 150µm was estimated to take into account the thickness of the AlGaAs/GaAs channel and metallic layers of Co, Cr and Au. Assuming an etching rate of 2.33µm/min as calculated on page 64, at least 60 minutes would be required for etching.
- After 75 minutes of etching, the step height from the window to the top of the photoresist was only 107µm.
- As the etching solution was believed to have a limited lifetime, a fresh mixture was prepared and etching was allowed to continue for a further 20 minutes.
- An etch depth of 120µm was now observed.
- The sample was then repeatedly etched and measured in 20 minute cycles for a total of three hours, and no significant change in etch depth was measured. However, a large amount of the wax adhesive became detached from the slide leading to contamination of the sample and to etching at the unprotected edges. It was decided that due to the apparent

solubility of the wax in ammonia, photoresist would be used as the adhesive during this stage in subsequent work.

- The sample was cleaned in acetone and IPA and then stuck to the slide using photoresist.
- Global etching was performed for another two hours in the ammonium solution until several smooth translucent patches appeared in the sample with a measured etch depth of around 140µm. The rest of the surface was extremely uneven and the edges of the sample in poor condition. The size of the sample had decreased substantially through edge etching. No attempt was made to remove the sample from the glass due to its fragility.

Following this stage, it was concluded that the etching rate through a small window decreases with depth and hence the time required is very large for a 150µm etch. It was decided that the sample would be globally thinned to 100µm in subsequent runs to avoid the long etching time and edge attack associated with the ammonium based solution. However, the ability to form a membrane had been demonstrated, thus achieving the goal of the stage.

7.7.6 Metallization of Bottom Surface

To extend upon the success of the membrane experiment, the ferromagnetic and capping layers were deposited on the etched surface.

- The glass square was suspended between two full glass slides, with the sample facing downwards.
- Two separate tungsten coils were loaded fully with permalloy.
- The pressure was reduced to 1.5×10^{-6} mbar and the permalloy was evaporated at 30V for each coil until it broke. A thickness of 18.1nm was recorded on the deposition monitor, which was sufficient for demonstrating these techniques.
- The broken coils were removed and replaced by a pair of tungsten boats used to hold gold and chromium respectively. Similar quantities of metal were used to those on the top surface.

- The pressure was reduced to 1 x 10^{-6} mbar on this occasion in an attempt to increase the evaporation rate thus allowing increased deposition of gold before the boat broke.
- At 22V, the chromium began to glow and at 30V, evaporation commenced. A 21.5nm layer was deposited before the metal ran out.
- The chamber was depressurized to 1 x 10^{-6} mbar.
- At 28V, the gold melted and at 35V, evaporation commenced. A 162.4nm layer was deposited before the boat broke once again.
- It was decided that to avoid wasting gold supplies, fabrication would be terminated at this stage.
- Observation under the optical microscope revealed a poor quality gold film over the uneven surface of the sample; however, the chromium layer appeared to be continuous (Figure 40).

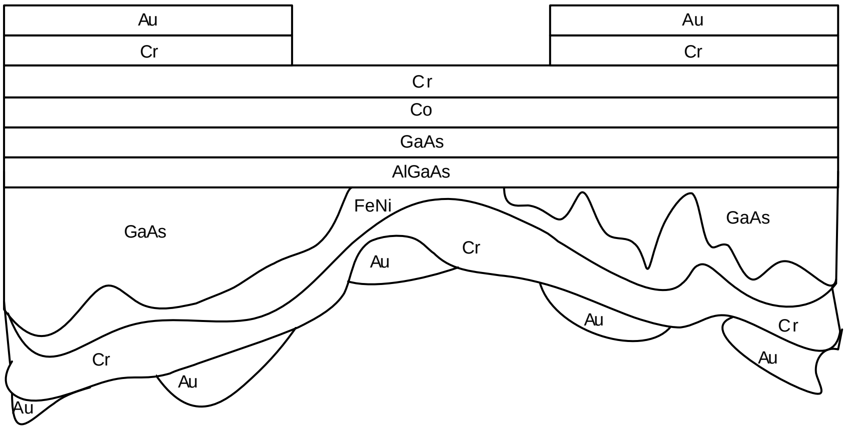

Figure 40: Approximate Representation of Final state of 080600:B1S1.

It was assumed that by etching to 100µm and hard baking the photoresist prior to etching the window, the problems resulting from the uneven surface would be resolved.

8 Spin-Valve Fabrication

Having established the necessary techniques, the fabrication of hybrid spin-valve structures commenced. Several iterations were performed, as techniques required modification or handling errors occurred.

8.1 Sample Identification

The remainder of sample 080600 was used in two batches to create seven individual extra samples. These sample numbers are identified in Figure 41.

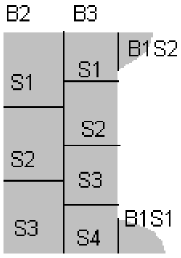

Figure 41: Sample Numbering for 080600

For the MBE experiments, sample C1773 was divided into five samples as shown in Figure 42.

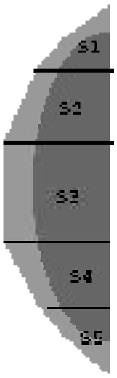

Figure 42: Sample Numbering for C1773

8.2 Fabrication Using Sample 080600, Batch 2

The three samples taken from 080600 are represented approximately in Figure 43 and Figure 44.

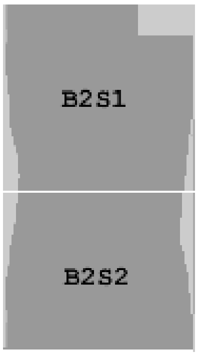

Figure 43: 080600, Batch 2, Samples 1 and 2

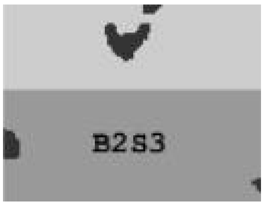

Figure 44: 080600, Batch 2, Sample 3

All three samples are shown with the metallic side upwards. These samples were non-ideal, as there were several uncoated areas, shown in a lighter grey. These defects were due to overlap with the sample holder used during deposition. Sample three bore several surface defects, shown in darkest grey.

Initially, all three samples were coated with capping metallic layers. Sample three was returned to the desiccator, whilst one and two were taken through an entire fabrication cycle. Measurements were attempted on the competed devices, although neither appeared to be functional. Processing was attempted on the third sample, but it was damaged irreparably and then discarded.

8.2.1 Metallization of Samples

A thickness of 50nm of chromium and 300nm of gold was considered adequate for packaging requirements on the smooth metallic surface of the sample.

- All three samples were cleaned and mounted upon a glass slide using photoresist as the adhesive on the GaAs surfaces.
- The photoresist was hard baked for ten minutes, and the slide placed in the evaporator with the samples facing the evaporation source.
- A 0.0685g piece of Chromium and 0.712g of Gold wire were placed in tungsten boats. It was later discovered that a 5mm piece of the gold wire had fallen out of its boat whilst replacing the bell jar on the evaporator.
- The pressure was reduced to 2.5 x 10^{-6}mbar and the Chromium was evaporated at 35V, yielding a deposition thickness of 51.9nm according to the deposition meter. This thickness exceeded the requirements.
- The pressure was reduced to 2.5 x 10^{-6}mbar once again and evaporation of the gold began at around 35V. After 234nm had been deposited, the crystal monitor connected to the deposition meter became ineffective.
- The chamber was returned to atmospheric pressure and the rate meter crystal replaced. 0.2231g of gold wire was placed into the boat and the pressure was brought back down to 2.5 x 10^{-6}mbar. Again, evaporation occurred around 35V and a thickness of 95.4nm was recorded on this occasion, bringing the total thickness to over 329nm, which exceeded the requirements.

The metallization of batch two of sample 080600 was therefore considered a success.

Fabrication of devices using samples B2S1 and B2S2 therefore continued, whilst B2S3 was kept as a spare.

8.2.2 Global Etching of B2S1 and B2S2

It was decided on page 66 that the well-established $H_2O:8H_2O_2:H_2SO_4$ etching solution would be used for the initial etching. To reduce the time required when using the ammonium based solution, the sample was to be etched down to 100µm globally.

During this stage, it was decided that to reduce the risk of the sample being damaged later by the mask aligner, a thin microscope cover slip would be used in preference to a thick glass slide. The specifications for the mask aligner show that a total sample thickness less than 2mm is preferable[55], and this was readily achieved by using cover slips.

- The samples were removed from the slides by dissolving the photoresist in acetone.
- They were then cleaned and stuck to thin microscope cover slips using wax, with the metallic sides facing the glass.
- The height of the centre of the top face of the sample above the glass was measured and the thickness of the wax at the edges was subtracted to gain an estimate of the sample thickness (Figure 45). This was inevitably a low estimate as the wax forms a raised lip around the edge of the sample.

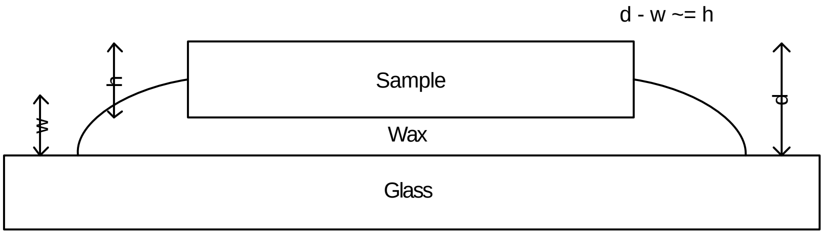

Figure 45: Illustration of approximate thickness measurement method

- A mixture of $H_2O:8H_2O_2:H_2SO_4$ was prepared and the height of the wax above the sample measured optically for each sample.
- Etching was carried out in several stages. The approximate height measurement taken over time is shown in Table 10 and Table 11.

Time (minutes)	**Measured Height, d (µm)**	**Approximated Thickness, h (µm)**
0	484	432
10	420	368
20	390	338
40	354	302
70	230	178
90	180	128
100	164	112

Table 10: Etching of 080600B2S1 in H_2O:$8H_2O_2$:H_2SO_4

Time (minutes)	**Measured Height, d (µm)**	**Approximated Thickness, h (µm)**
0	480	444
10	406	370
20	364	328
40	310	274
70	200	164
90	170	134
100	110	74

Table 11: Etching of 080600B2S2 in H_2O:$8H_2O_2$:H_2SO_4

8.2.3 Photolithography on B2S1 and B2S2

- The samples were removed from the wax with acetone and cleaned.
- The samples were stuck back onto the cover slips using photoresist.
- Photoresist was spun onto the samples and baked on as described previously.
- A 200µm square was exposed onto B2S1 and a 200µm diameter circle onto B2S2. The use of cover slips instead of glass slides appeared to be a success as breakage did not occur under the mask-aligner.
- Optical microscopy revealed a well-defined square upon each sample aligned with the [110] direction.

8.2.4 Selective Etching on B2S1 and B2S2

Prior to selective etching, the sample was subjected to a brief reactive ion etch (RIE) using oxygen ions to remove any excess photoresist from the window area. The settings used are shown in Table 12:

Parameter	**Value**
Power	5W
Pressure	120mTorr
Time	1min
Flow Rate	5sscm

Table 12: Settings for O_2 Reactive Ion Etch

Optical microscopy revealed a clean, well-defined aperture on each sample.

To reduce the time taken for selective etching, another fast etch step was used to remove 48µm over ten minutes.

During the selective etching, air was constantly bubbled over the samples to remove residues from the etching process. The etch depth remain constant at around 114µm after 20min, although the windows appeared to widen slightly over the next 15min. Optical microscopy revealed a relatively smooth membrane, which appeared slightly translucent.

8.2.5 Metallization of B2S1 and B2S2

- As a variation on the use of permalloy, nickel was evaporated onto the sample. The original intention of evaporating 30nm of nickel failed as the wire filament broke after only 5nm had been deposited. The second filament in the chamber was used to evaporate 6nm of chromium to prevent oxidation of the nickel.

- The photoresist was dissolved in acetone, and the lift-off appeared to be successful under optical microscopy.

- The samples were stuck back onto glass slides using photoresist for the final metallization step.

- In order to economise on the large amount of gold required to form the capping layer, aluminium was used from this point forward. The evaporation chamber was depressurised to 3 x 10^{-6} mbar and aluminium was evaporated from two filaments in immediate succession to form a complete thickness of 285nm.

- The samples were removed from the glass slide using acetone and observed using optical microscopy. It appeared that a discontinuity in the metal film existed around the aperture on each sample.

8.2.6 Packaging of B2S1 and B2S2

- The samples were stuck onto a chip-holder using conductive silver paint, with the etched side uppermost.
- In an attempt to compensate for the discontinuity in the aluminium film on the top surface, a small drop of silver paint was placed over each window.
- The ultrasonic wire bonder was used to form several bonds between the chip holder and the ground plane and between the chip holder and the top of each sample using the parameters shown in Table 13.

Bonding area	**Force**	**Time**	**Power**
Chip Holder	1.5	3	1.5
Sample	3	3	1.5

Table 13: Bonding parameters for 080600 B2S1 and B2S3

The layout of the bonding is shown in Figure 46. The chip holder is compatible with the MR measurement equipment. It is designed to fit into the equipment with the samples facing downwards. The pins are therefore numbered anticlockwise from the marked corner. Pin 18 was slightly extended for identification purposes. Five bonds were formed between the chip holder and the ground plane, two between the chip holder and the top surface of sample B2S2 and five between the chip holder and the top surface of sample B2S1.

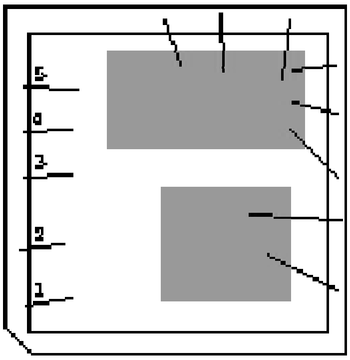

Figure 46: Bonding Configuration for B2S1 and B2S2

8.2.7 I-V MR Measurements on B2S1 and B2S2

The sample was mounted in the MR measurement equipment and a multimeter was connected between each of the top and bottom contacts of sample B2S1. Measurements between ground plane contacts showed a resistance of 0.1O and measurement between pins on the top surface of either sample showed a resistance of 0.6O implying that the wire bonds were of sufficiently high quality.

Measurement between the top surfaces of the two samples revealed a problem with the packaging method. A short circuit was observed between the tops of the two samples, implying that an electrical bridge existed between them. To remedy the problem, a diamond scriber was used to remove the excess silver paint between the samples. Repetition of the measurement showed an open circuit between the tops of the samples allowing measurement now to take place.

The “top to bottom” resistance measured for B2S1 was 23MO when initially connected. This however suddenly rose to an approximately infinite value. For B2S2, a very small resistance of 7.4O was observed.

Trial sweeps of magnetic field upon each sample revealed only a low-level noise pattern, implying that both devices were defective. Both samples were removed from the chip holder by dissolving the silver paint in acetone and breaking the wire bonds with tweezers. Optical microscopy revealed a hole in the membrane on each sample. This shows that the small resistance measured in B2S2 was in fact that of the silver paint creating a rough contact with the ground plane through the membrane. It is possible that the application of silver paint to the top of the membrane damaged it irreparably. This may be due to either excessive force being applied during the application or to the thermal contraction resulting from evaporation of the solvent.

In B2S1, as the measured resistance changed rapidly it is likely that the membrane was destroyed by the measurement process. This implies that the multimeter supplies excessive current to the device during automatic resistance measurements.

To avoid damage to future samples, several decisions were made:

- The need for an application of silver paint to the membrane would be negated by the formation of a continuous metal film across the aperture. To achieve this, subsequent evaporations were performed with the sample angled away from parallel with the source material. The gradient of the sides of the window is therefore decreased relative to the direction of flow of metal atoms.
- To reduce the probability of damage to the membrane due to thermal contraction, subsequent samples were left overnight to cool radiatively under vacuum after evaporations had been performed.
- Measurements of resistance were performed using only the new Keithley sourcemeter equipment set to source a low current and measure voltage. The automatic resistance measurement was found to have too small a range and to supply excessive current in all available multimeters.

8.2.8 Global etching of B2S3

B2S3 had been kept as a spare sample, with the back-surface metallic layers already deposited. It was therefore a relatively short process to complete device fabrication.

- B2S3 was cleaned following the method previously defined.
- The sample was mounted on a thin glass cover slip using wax, with the metallic face downwards.
- A small quantity of photoresist was deposited around the edges of the sample to prevent excessive etching to the exposed sides and was baked on for ten minutes at 115^{o}C.
- A $H_2O{:}8H_2O_2{:}H_2SO_4$ etching solution was prepared and etching was performed in several stages. The thickness of the sample above the top of the wax layer was measured, although on this occasion, it was decided that the sample would be left slightly thicker to avoid damage by the mask aligner. By stopping at a measured thickness of 100µm above the wax layer, the actual sample thickness would be around 130µm, as with previous samples. The measured thickness of the sample over time is shown in Table 14.

Time (minutes)	Measured Height, d (µm)
0	540
10	500
20	465
60	240
100	100

Table 14: Etching of Sample 080600B2S3 in $H_2O{:}8H_2O_2{:}H_2SO_4$

8.2.9 Photolithography of B2S3

In this stage, the intention was to expose a square window onto the sample at 45° to the edges. By doing this, the window would be etched away along lines, which were not parallel to the crystal planes. This would create an approximate octagonal window, which may result in a more marked anisotropic effect in the magnetisation of the two parallel magnetic films.

- Positive photoresist was spun on at 3000rpm for 45s and baked on for one minute at 115°C.
- A 100µm square window was defined in a positive mask using the method described on page 74.
- The sample was brought into contact with the mask at a force of 300g, but once again, the sample was cracked during contact. It was therefore decided that the contact force must be lowered still in further work.
- Due to the damage to the sample, it was rejected and work was terminated.

8.3 Fabrication Using Sample C1773, sample 3

The largest piece of C1773 (sample 3) was chosen for use in device fabrication. All other pieces were returned to the desiccator for safekeeping.

8.3.1 Global Etching of C1773S3

- Sample 3 was cleaned and mounted onto a glass cover slip with wax. The epitaxially grown layers faced downwards as in previous experiments.
- The sample was etched in a 1:8:1 fast etch solution for an hour. Optical microscopy was performed using the method of approximating the thickness of the material described previously. The results showed that the sample had a thickness varying from 45µm in one corner to 310µm in the opposite corner.
- The sample was removed from the glass and was cleaned. Repetition of the thickness measurement confirmed the slanted geometry. It is unclear why the sample etched in this manner, although it is possible that either

the composition of the material or its initial geometry led to a gradient of etching rates across the length of the sample.

8.3.2 Photolithography of C1773S3

As this was to be the first attempt at using MBE growth, a large circular aperture was defined in this stage. This aperture would be clearly visible with optical microscopy allowing the membrane to be inspected thoroughly and the method to be validated.

- The sample was stuck onto the glass cover slip using photoresist and hard-baked for ten minutes.
- Photoresist was spun on at 3000rpm for 40s and soft-baked.
- A 400µm diameter circle was defined in a pair of masks and the sample was brought into contact with the mask with the minimum force of 200g. Once again, however the sample was broken in the process although enough remained for a 7s exposure to be performed on a thin strip of material. It was decided that the equipment must be used in proximity mode in future experiments to prevent breakage.
- The photoresist was developed for 45s and optical microscopy revealed a well-defined 400µm diameter circular aperture.

8.3.3 Selective Etching

- A plasma etch was performed to remove the excess photoresist from the membrane. The settings used were identical to those in previous experiments.
- The circular window was etched for ten minutes in the fast etch solution to reduce time taken for selective etching. Optical microscopy revealed that an etch depth of 100µm had been achieved. The surface appeared to be smooth and flat over the full window region.
- The sample was then subjected to a 30min selective etch. Optical microscopy now revealed an etch depth of 160µm. A small hole was visible in the membrane, resulting in the rejection of the sample. The remainder of the membrane however was very well defined, with a relatively shallow edge gradient and a completely smooth, translucent surface. It was decided that future work on this type of device would be

worth pursuing although care was needed as the etch rate appeared to be very high.

8.4 Fabrication Using Sample 080600, Batch 3

8.4.1 Sample Preparation and Metallization

- The remainder of sample 080600 was scribed into four pieces along the GaAs face, although cracking was not performed at this stage.
- The scribed sample was placed between two glass slides, supported only on the corners. A small piece of masking tape was used to secure the sample in its position (Figure 47).

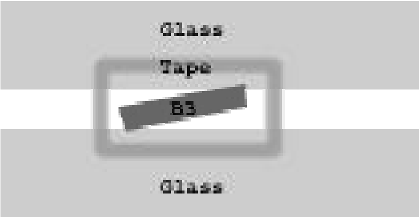

Figure 47: Sample Holder for Evaporation onto 080600B3

- A thickness of 300nm of aluminium was evaporated at a pressure of 1.5 x 10^{-6}mbar. This was somewhat less than the target of 400nm, but was considered sufficient for packaging to take place.
- The sample was then cracked down the centre line into two pieces. One piece, carrying samples B3S3 and B3S4 was returned to the desiccator, whilst the other piece was cracked again to yield two separate samples – B3S1 and B3S2.
- Samples B3S1 and B3S2 were cleaned once again.

8.4.2 Global Etching of B3S1 and B3S2

The two samples were etched in a $H_2O:8H_2O_2:H_2SO_4$ solution using the method described on page 81. The measured thicknesses are shown in Table 15 and Table 16.

Time (minutes)	Measured Height, d (µm)	Approximated Thickness, h (µm)
0	490	430
65	140	80

Table 15: Etching of 080600B3S1 in H_2O:8H_2O_2:H_2SO_4

Time (minutes)	Measured Height, d (µm)	Approximated Thickness, h (µm)
0	545	430
65	265	150
80	190	75

Table 16: Etching of 080600B3S2 in H_2O:8H_2O_2:H_2SO_4

8.4.3 Photolithography

In order to reduce the probability of the sample being broken during this phase, optimal settings were found in the equipment manual. These are outlined below.

Firstly, it is important to use the equipment in "Alignment Mode" as opposed to "Manual Mode." This causes the microscope to be moved away from the mask area allowing easy access. The sample is also raised at a much slower rate, and confirmation is sought before the chuck motion begins.

The parameters must be set as in Table 17, prior to loading the sample.

Parameter	Value	Description
`Vacuum Chamber`	`0`	Deactivates the vacuum between the sample and the mask
`Substrate Vacuum`	`1`	Activates the vacuum between the sample and the chuck
`Proximity`	`1`	Runs the equipment in proximity mode
`Separation Time`	`Default`	Only used during automatic operation

Proximity/ Contacts=n	20	Sets the distance between the mask and the sample at 20μm
Separation	Default	Only used during automatic operation
Exposure Time	7	Sets 7s exposure
Contact Force	200	Sets 200g initial contact force between sample and mask

Table 17: Optimal Mask Aligner Settings

These settings taken in their order of appearance initially deactivate the vacuum between the sample and the mask. As the samples generally have a slightly concave surface due to the edge protection in the global etching, a vacuum applied to the top surface is likely to pull the centre of the sample upwards and thus cause a fracture. The vacuum between the substrate and the chuck is preserved to avoid lateral movement of the sample during alignment. The mask aligner is then set into proximity mode, which initially brings the sample into contact with the mask at a contact force of 200g to ensure parallelism. The sample is then moved away from the mask to a distance of 20μm. It was assumed that the brief contact force of 200g and the deactivation of the vacuum would be sufficient measures to avoid fracturing the samples.

- Photoresist was spun onto the two samples at 3000rpm for 40s and baked on for 1min at 115^{o}C.
- A 100μm square window was defined on the pair of masks and exposed onto the surface of sample B3S1.
- The photoresist was developed for 45s and observed under the optical microscope. A well-defined square was visible, and no evidence of breakage could be seen.
- The photoresist was hard-baked for 10min at 115^{o}C.
- The process was repeated to define a 100μm circular window on sample B3S2. This was also entirely successful.

It was therefore decided that the mask-aligner settings defined above were adequate for the purposes of this project. It is important to note however that by using the equipment in proximity mode, the level of diffraction of UV around the mask is increased[56]. Therefore for the definition of very small features or when using a short wavelength lamp, significant blurring of edges would occur and an alternative method would be required.

8.4.4 Selective Etching

To prepare the sample for selective etching, a plasma etch was used to remove excess photoresist from the aperture as described previously. Observation with optical microscopy showed a clean aperture defined in the photoresist for both samples.

- A $40H_2O_2:NH_4OH$ etching solution was prepared and etching was performed in several stages. At each stage, the step height into the aperture was measured optically. This time, the solution around the sample was not agitated during the etching process.
- The etch depth of each sample over time is shown in Table 18 and Table 19.

Time (min)	**Etch Depth (µm)**
25	30
50	55
60	55
70	55
80	60

Table 18: Etching of sample 080600B3S1 in $40H_2O_2:NH_4OH$

Time (min)	**Etch Depth (µm)**
25	35
50	50
60	75
70	80
80	80

Table 19: Etching of sample 080600B3S1 in $40H_2O_2:NH_4OH$

- Optical microscopy of sample B3S1 revealed a flat, translucent AlGaAs membrane, covering around 70% of the window area. The window of sample B3S2 however showed an irregular surface even after an additional two hours of etching. It was suggested that the irregular surface was due to the deposition of a residue of the etching process, and that this may be eliminated by constantly agitating the solution, surrounding the sample with a stream of air bubbles using a pipette, as in the fabrication trials.

It was therefore decided that sample B3S1 was ready for deposition of the ferromagnetic layer, whilst B3S2 would need further work to create an acceptable membrane first. B3S2 was returned to the desiccator for safekeeping.

8.4.5 Metallization of B3S1

Two tungsten filaments containing around 4cm of permalloy wire each were used to evaporate a total of 31.1nm of metal onto the membrane at a pressure of 6 x 10^{-6}mbar. Note that during this stage, the photoresist was left on the surface of the GaAs. This effectively decreased the depth of the window, reducing the probability of discontinuities in the Al capping layer. It also ensured that the deposited permalloy would be in a square window and exhibit minimal shape anisotropy. The sample was left overnight to cool to avoid damage due to thermal contraction. When the sample was removed from the evaporator, it was found that the photoresist had bubbled somewhat. This is likely to be due to the long time during which the sample was held above the heated filament during evaporation. To reduce the chance of the sample dropping from damaged photoresist or from being contaminated, the metal must be allowed to begin evaporation at a high rate before the shutter is opened.

The photoresist was removed in acetone and the sample was observed with optical microscopy to confirm that a smooth, continuous layer of permalloy had been deposited over the membrane. The sample was then stuck to a glass slide using photoresist.

To avoid the problems experienced with batch 2 regarding the discontinuity in the deposited metal layer, metallization of B3S1 was performed with the sample at a slight incline. To achieve this, two glass slides were placed under one side of the sample, whilst three were placed under the other. The sample was secured with a small piece of masking tape.

Two tungsten coil filaments were filled with 6cm of aluminium wire and the metal was evaporated at a pressure of 1.2 x 10^{-6}mbar to form a 900nm thick layer on top of the GaAs. The sample was left to cool overnight and removed from the evaporator. Optical microscopy revealed a smooth continuous layer of aluminium on top of the GaAs, with no observable discontinuity at the window edge.

8.4.6 Packaging of B3S1

The sample was bonded to a chip holder using silver conductive paint. Several wire bonds were made between the pins and the ground plane and from the pins to the top of the device as shown in Figure 48, using the parameters shown in Table 20.

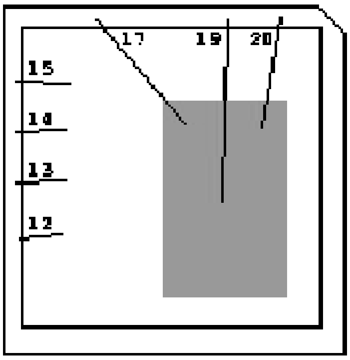

Figure 48: Packaging layout of B3S1

Bonding area	Force	Time	Power
Chip Holder	1.5	3	2
Sample	2.5	3	1.3

Table 20: Bonding Parameters for B3S1

The quality of the bonding was tested by measuring the resistance between each of the grounded pins. In all cases, the resistance was below 0.1O. The resistance between each of the pins connected to the top of the sample never exceeded 1O, which showed that the quality of the bonds and of the metal film were sufficient to allow further measurements to take place.

8.5 Testing of B3S1

Tests were performed upon sample B3S1 to investigate its electrical and magnetic behaviour.

8.5.1 I-V Characteristics

As the predicted impedance of the device was high, it was essential to consider the experimental apparatus carefully to avoid inaccurate results. It was decided previously that to avoid damaging the device, its current flow must be limited. The simplest method to achieve this was to apply a current source to the device.

By measuring the voltage dropped across the device, it was possible to plot the current against voltage and hence the static resistance against voltage curves.

Current was passed through the sample from the permalloy side down to the cobalt side using a Keithley sourcemeter. The advantages of using this device were its high output impedance and wide range of source and measurement values. A 30V voltage limit was set to restrict the maximum power dissipation in the device. Current was sourced within this limit for the device in its reverse biased regime. For the forward biased regime, the current was limited to 5µA for the same reasons.

The voltage was recorded for this range of currents and the results inverted to form a graph of I-V characteristics (Figure 49). This was found to be repeatable for all connections to the device. The characteristics are clearly similar to those of a schottky diode. This implies that the schottky barrier height for one of the metallic layers dominates the response within the current range observed. This is advantageous to measurements as the static resistance of the device may effectively be reduced by increasing the forward supply voltage. This prediction is confirmed by dividing the observed voltages by their corresponding currents. The results are shown in Figure 50 and Figure 51.

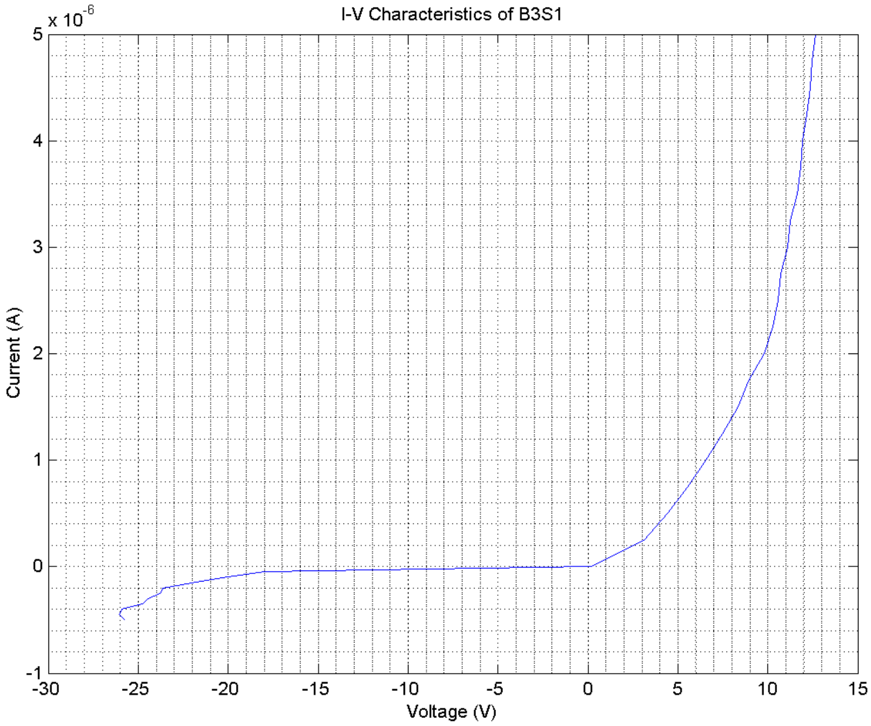

Figure 49: I-V Characteristics of B3S1

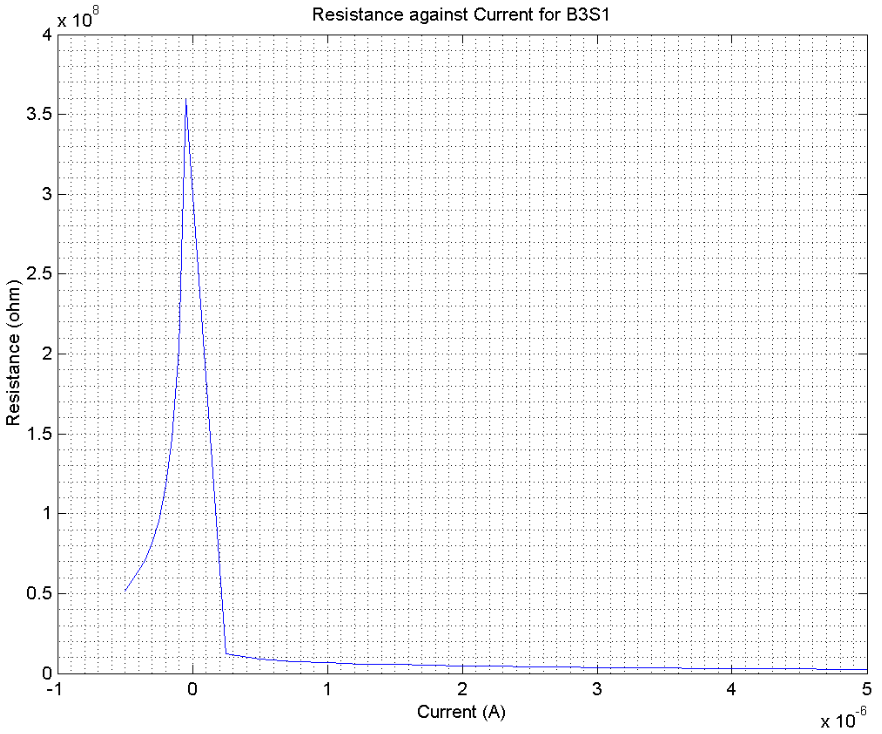

Figure 50: R-I Characteristics of B3S1 (full scale)

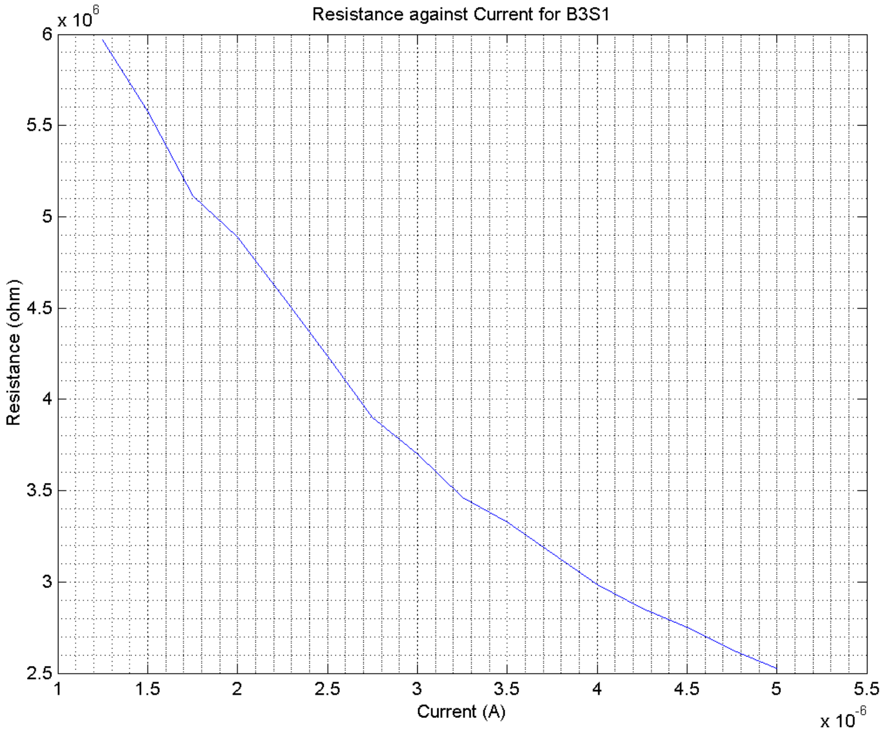

Figure 51: R-I characteristics of B3S1 (positive current only)

The quality of the interface between the metal and semiconductor can also be deduced from these results. The reverse breakdown voltage is high at around 25V and the reverse leakage current is low (around 50nA). This implies that the effect of surface states due to imperfections is low and that a smooth, intimate contact exists.

8.5.2 Magnetoresistance Measurements

To reduce the electrical resistance of the device, whilst not causing excessive power dissipation a constant current of 10µA was supplied to the device. To reduce the effect of thermal noise, a 100-point repeat filter was applied to the measurements. The sample was aligned along its hard axis in a variable magnetic field. Voltages between -0.8V and +0.8V with a 0.05V step were applied to the magnet, with 20s allowed for each measurement to be made. A computer controlling the magnet recorded the magnetic field values at each point, whilst a Keithley sourcemeter was used to record the voltage across the device and supply the bias current. The results are shown in Figure 52.

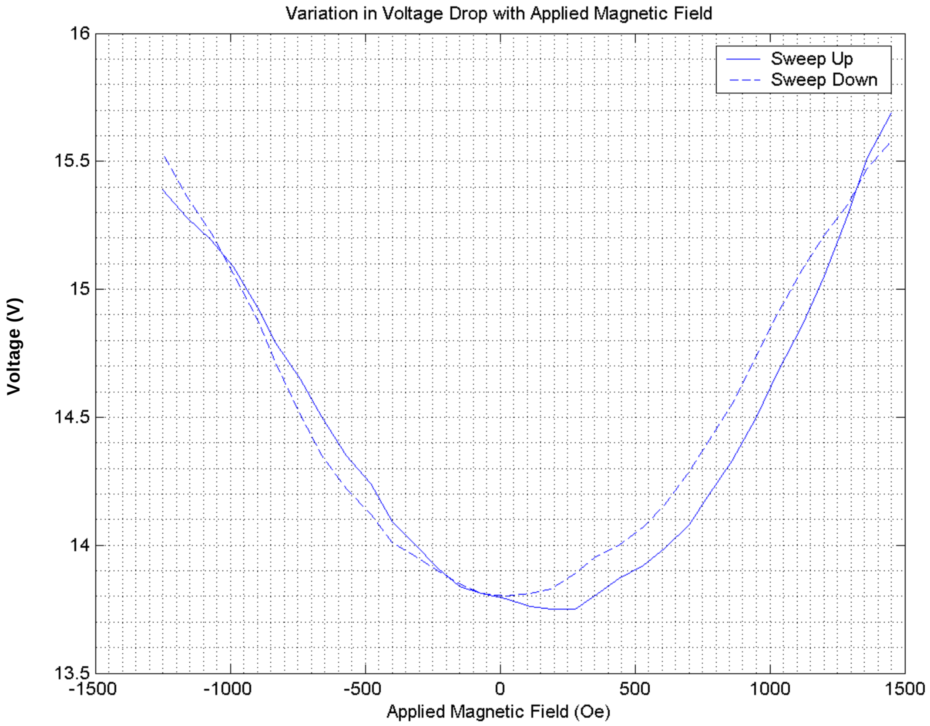

Figure 52: Voltage Drop against Field for B3S1

By subtracting the minimum voltage recorded from each of the measurements and then dividing by this minimum value, the magnetoresistance ratio was plotted in Figure 53. These graphs show a minimum resistance of 1.415MO for an applied magnetic field of 200Oe.

It is clear from the data that significant magnetoresistive effects of up to 14% exist in the device. It was however, the opinion of Dr Ahmad that the observed graph showed AMR rather than GMR effects, as independent switching of the ferromagnetic layers was not observed. In previous MOKE measurements, it was shown that the coercivity of sample 080600 was around 70Oe along its hard axis and hence a large variation of resistance around this value would be observed for the GMR effect.

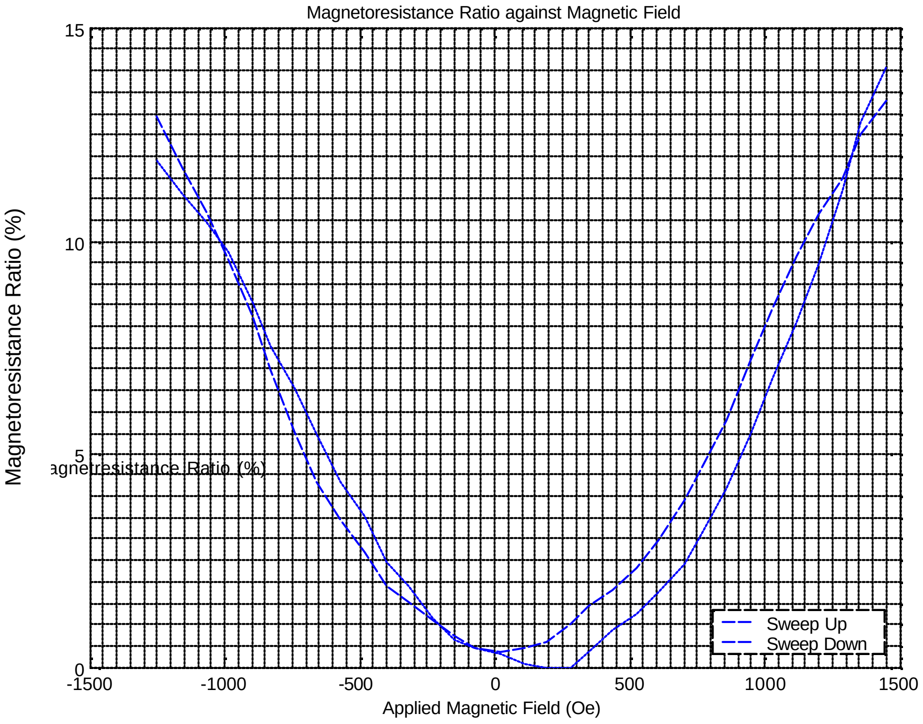

Figure 53: Magnetoresistance Ratio of B3S1

9 Further Work

Ultimately, the limiting factor in the practical aspect of this project has been time. Impressive, reproducible results have been obtained from sample B3S1, which implies that further work in this research area will be extremely valuable.

Initially, it would be beneficial to add experimental evidence for the large AMR measurements achieved by repeating the entire fabrication and measurement processes for B3S1. As well as proving the reproducibility of measurements for the entire process, this will finalize the fabrication process. Future devices may then be produced rapidly and with a high yield, thus allow a higher throughput of testable hybrid spin-valves.

A natural progression from this work will be the fabrication of devices with varying dimensions of ferromagnetic contacts. By using rectangular and circular windows, the effects of large and small levels of anisotropy may be investigated. The resistance of the device as a function of area may also be investigated.

The use of MBE growth for both ferromagnetic layers is another progression from this project. The resulting quality of the metal-semiconductor interfaces is likely to be superior to that achieved by evaporation, allowing better control of schottky barrier heights. Due to time constraints, MBE growth was not attempted although the preliminary fabrication methods have been investigated. Sample C1773 appears to show good quality selective etching in experiments although care will be required to ensure that the membrane is not broken by excessive etching. Prior to MBE growth, argon sputtering may be used to remove impurities from the substrate surface. An EPSRC research proposal by Dr Xu also suggests the removal of the AlGaAs layer in a second selective etching stage using hydrofluoric acid. These steps would allow for better prediction of the device characteristics as the channel will consist entirely of GaAs without the addition of AlGaAs and impurities. The MBE growth may be performed to set the directions of the magnetic axes of the two ferromagnetic layers relative to each other, allowing investigation into the effects of lattice anisotropy.

To investigate whether GMR exists in these hybrid structures, it will be necessary to repeat the magnetic measurements across a full rotation of the magnetic field direction with respect to the device geometry. Extremes of magnetoresistance ratios are expected along the hard and easy axes of the cobalt layer.

Further experimentation will reveal the level of current dependence of the magnetoresistance. It is expected that by increasing the forward current through the device, the interface resistance will decrease exponentially whilst the magnetoresistance will remain approximately constant. Thus as the current increases, the magnetoresistance ratio will increase rapidly.

One of the novel predictions of this report is that of frequency dependent spin-injection. As large AMR values have been observed in the sample and GMR effects may yet be observed, it is likely that frequency-dependence will be observed. Investigation is therefore necessary in order to prove the existence of this effect. Using the method described in section 6.3, the total resistance of the device may be measured over a large frequency range using a network analyzer. The frequency-dependence may be investigated fully by varying the current and field directions as described above in conjunction with network analysis.

It is the author's opinion that the level of experimental investigation described up to this point will be within the scope of an MEng project over a period of six months. If the fabrication techniques described in this report are used as a basis for experimental work, the rate of production of testable devices will be high from the outset.

Direct measurement of the spin-injection into the device is difficult using the structures fabricated in this project. However, the incorporation of a quantum well into the device will create a spin-LED structure, which allows emission of photons within the active area of the well. Due to the recombination of spin-polarized carriers, a net polarization of photons will be observable for a spin-polarized current. By this method, the spin-injection into similar devices to those in this report may be investigated during the experiments described.

A further modification in device structure would be the incorporation of a 2DEG channel in an InAs/InAlAs heterostructure. This structure, similar to that of the Datta-Das Spin-FET, would offer higher electron mobility. It is likely therefore to yield higher magnetoresistance.

Ultimately, in the pursuit of creating a working Spin-FET, a lateral device geometry must be achieved. This will allow the addition of a gate contact to the device. This will be a continuation of the work by Simon Hees[57] at York, in which a thorough investigation into the lithographic techniques required for fabrication was performed. The variation of dimensions due to the proximity effect proved a major obstacle and parameters for e-beam lithography must be carefully selected before devices may be fabricated in large quantities.

Once the lateral device has been fabricated and tested thoroughly, a gate contact may be added to the structure between the source and drain contacts as suggested by Datta and Das. A major technological challenge will be the isolation of the three contacts from each other at such small separations. A material with an extremely large dielectric constant will be required between the contacts to prevent tunnelling. A starting point would be the growth by PECVD of silicon dioxide between the contacts, although better dielectrics may well be required.

Initial testing of the completed Spin-FET will involve measurements of the magnetoresistance across a wide frequency and current range for the hybrid spin-valve. A gate voltage perpendicular to the 2DEG channel must then be applied in order to investigate the presence of the Rashba effect in the device. Assuming a high level of spin injection and detection, the detected current should decrease as the gate voltage rises provided the magnetization of the source and drain be aligned. Conversely, the detected current should increase as the gate voltage rises when the magnetization of the source and drain contacts are antialigned.

Following a full investigation into the operation of the Spin-FET, work will be required to develop design rules for the use of Spin-FETs in electronic systems. In other words, equations relating drain current to gate-substrate voltage and relative magnetization of the source and drain are needed. The Ebers-Moll equations for bipolar transistor are good examples of this type of equation.

Before commercial fabrication, analysis of the absolute limits on performance of the Spin-FET must be carried-out. The maximum operating currents must be tested for each contact as well as the limits on applied voltage and power dissipation. The operating temperature range and effective noise model must also be established.

Naturally, the latter recommendations are somewhat less specific than the former as intermediate discoveries will have a major bearing upon the work required in these stages. It is the author’s intention to make realistic and realisable recommendations for further work rather than to speculate. As such, by following the former recommendations, a greater level of specificity will be made possible in the latter and the quest for a working Spin-FET will draw closer to its conclusion.

10 Conclusions

The desirability of hybrid spin-valve structures was discussed in this report in considerable depth. The working device fabricated as part of this project shows potential in its own right as a Spintronic magnetic field sensor exploiting AMR effects. By applying a fixed current of 10µA to the sample from the permalloy layer to the cobalt layer, a variable voltage is visible depending on the applied magnetic field. Furthermore, placing the device at the input to a comparator referenced against a potential divider allows the device to be converted to the digital domain (Figure 54). The device is adjustable by means of a potentiometer. This allows the field at which the comparator switches to be controlled.

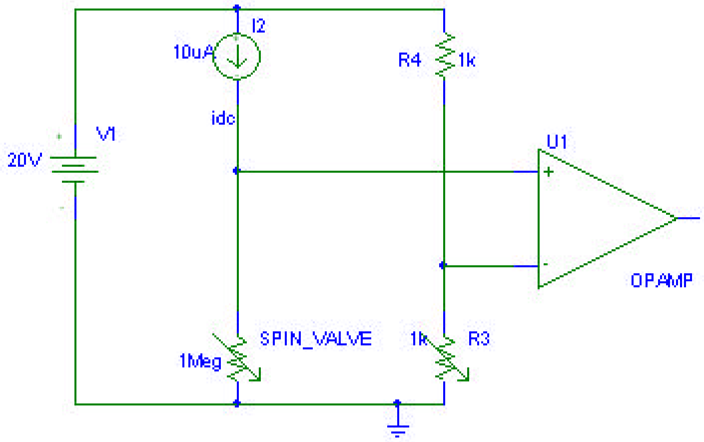

Figure 54: AMR Magnetic Field Sensor using B2S1

The intention of the practical aspect of this project of course was to observe the GMR effect in a hybrid spin-valve structure. It must be stressed that further investigation of device B3S1 may reveal GMR behaviour in further testing as suggested in section 9. Time constraints however have precluded extensive tests or fabrication of further devices.

The prediction in this report of high dc impedance for devices has been confirmed by the measurement of I-V characteristics, although the schottky diode effect of the metal-semiconductor barriers has allowed much lower resistance to be observed at higher forward currents. It has yet to be seen whether the impedance of the device is frequency dependent as predicted by analysis of the parasitic parameters of the equivalent circuit model. The capacitive nature of the device is implicit in its schottky response however and it is likely that frequency dependent conductivity will exist.

The yield of successfully fabricated devices was understandably low as the fabrication techniques were being developed continuously throughout the practical work. This preparatory work however has firmly established reproducible methods of fabricating a hybrid spin-valve such as B3S1. Initial difficulties including breakage of samples in the mask-aligner and contamination of the etching solution have been overcome. At an industrial scale, devices such as this may be fabricated principally using automated methods to prevent variations due to a human operator[58]. It is therefore possible to achieve near to 100% yield of devices commercially.

The cost of such devices will also be relatively low, as they will be fabricated in large batches on GaAs wafers. A typical 75mm GaAs wafer costs around £70 although wafers with an epitaxially grown quantum well structure may cost several times this amount. As the industry now uses 150mm GaAs wafers as a standard, with 225mm wafers becoming more commonplace the size of batches has grown and hence the labour costs are decreasing. A 150mm wafer has an area of approximately 70000mm^2, and as the area of the aperture is less than 1mm^2 in B3S1, it is feasible that a great many devices may be fabricated on a single wafer. The use of aluminium as a capping layer instead of gold and chromium also reduces costs considerably.

The theoretical aspect of this project has presented several novel perspectives on the applications of Spintronic devices. Whilst Spintronics is still in its infancy, the advances already yielded by the simple all-metal spin-valve have been dramatic. The speed and miniaturisation of field sensors have improved dramatically, whilst the majority of computer users now possess a Spintronic device on their desktop in the form of a GMR read-head. The next major advance will come in the form of MRAM, offering fast, non-volatile primary storage exhibiting high integration densities and temperature independence. Instant booting of computer systems will become possible in the near future as

MRAM chips reach capacities and costs, which permit their use as core memory (registers and on-chip caches) in microprocessors.

The ubiquity of the field-effect transistor is such that the Spin-FET may provide advances in many aspects of Electronics. This report presented an example application in the form of an all-digital magnetic field sensor. Its ability to mimic the characteristics of a wide range of FETs will allow reconfigurable digital devices to be fabricated. Reconfigurable microprocessors and programmable logic devices will be a natural progression from the development of the spin-FET. The potential is enormous for advances in the field of quantum computing, which will process data as a superposition of spin-states and in neural networking, where reconfigurable hardware will allow the realisation of perceptrons and other fundamental components. Self-healing systems will also be made possible with considerably less redundancy than current systems of this nature. A number of "spare" transistor blocks will be included in a system, and will be configured to replace a faulty block by application of magnetic fields through parallel current lines.

Both the MTJ storage elements within MRAM and the Spin-FETs within a reconfigurable microprocessor may be controlled by the application of magnetic fields. It is therefore conceivable that spin-based processing elements may be embedded in MRAM chips. Devices such as PIC microcontrollers may also incorporate MRAM as non-volatile data storage thus improving their capabilities as a computer on a single chip. The distinction between storage and processing elements will therefore become increasingly blurred and one of the great goals of Spintronics will be realised, benefiting industry and humanity alike – The Combination of the Hard Disk and the Processor.

Appendix I. MATLAB Simulations

Throughout this project, MATLAB simulations have been used to facilitate calculations. MATLAB is designed to process mathematical operations upon matrices in an efficient manner, and is able to plot graphs of vectors of data points. Commands may be combined into batches called "m-files", and used as functions. Graphical and textual user interfaces are available. In this appendix, program listings are given for each m-file used and commentary is included.

A. Analysis of MOKE measurements

An m-file called "`moke.m`" was written to convert a LabView data file to graphical data and calculate the coercivity of the sample. The function is written in full below.

```
function coerce = moke( filename )
%
% function coerce = MOKE( filename )
%
% Plots a graph of MOKE data from a data file returned by the
% MOKE equipment and prompts the user to click on the zero
% magnetization axis crossings.  The coercivity is then
% calculated and returned.
% The data file must be in standard 4-column format and must
% start with a letter.
%
% (c) Alex Valavanis 2004, University of York

try
  load( filename );                        % loads the file
  data = eval( strtok( filename , '.' ) );  % stores contents of
                                            % file as matrix
                                            % called "data"
catch                               % Rejects invalid files.
  error('***ERROR: File not found or Filename Invalid.  Filename
         must start with a letter, NOT a number.  Please rename
         file or choose another file then run this Function
         again.'
        );
end
```

```
% Extracts data into field and magnetisation vectors
field = [ data( 0 * length( data ) + 1 : 1 * length( data ) ) ,
          data( 2 * length( data ) + 1 : 3 * length( data ) ) ];
M     = [ data( 1 * length( data ) + 1 : 2 * length( data ) ) ,
          data( 3 * length( data ) + 1 : 4 * length( data ) ) ];

% Normalizes and centres magnetization vector
M     = M - ( max( M ) + min( M ) ) / 2;
M     = M / ( max( M ) );

% Plots graph and requests title from user
plot( field , M );
title( [ 'MOKE data from ' , filename ] );
xlabel( 'Field (kOe)' );
ylabel( 'Normalised Magnetisation' );
grid on;

% Allows user to zoom into M=0 region
disp(' ' );
disp('Zoom in to low magnetisation region and press any key to
      continue...'
     );
zoom on;
pause;
zoom off;

% Prompts user to select zero crossing points
disp( ' ' );
disp( 'Click once on each zero crossing point...' );
[ x , y ] = ginput( 2 );

% Calculates coercivity
coerce = ( max( x ) - min( x ) ) / 2;

disp(' ' )
disp( [ 'Calculation completed on ' , filename ] );

% End of Function
```

This function normalizes and centres the MOKE Voltage and hence the magnetization and then displays the hysteresis-loop. The user clicks on the two zero-magnetization axis-crossings and the coercivity is calculated and returned.

B. Graphing Coercivity

A second function in an m-file called "`graphcrc.m`" was created to graph the coercivity of the material against the direction of the applied magnetic field. The function is written in full below.

```
function graphcrc

% function GRAPHCRC
%
% Draws a graph of coercivity against direction of applied
% magnetic field.  The user may input a set of MOKE data files
% and pick the points corresponding to zero magnetization.  The
% coercivity graph is automatically generated after the last
% dataset is input.  Erroneous data may be removed via the GUI
% front-end of the function.
%
% (c) Alex Valavanis 2004, University of York

direct = [];  % Defines null vectors for direction and coercivity
coerce = [];
finished = 0; % Defines Boolean flag to allow exit of function.

while finished == 0 % Until user chooses to exit
  % Displays Drawing Menu with three options as shown:
  option = menu( 'Drawing Menu',
               'Add a file',
               'Remove last data',
               'Finished - Draw Coercivity graph!'
              );
  if option == 1            % "Add a file"
    fileok = 0;              % Sets Boolean OK flag

    while fileok == 0
      % Prompts user for filename
      disp( ' ' );
```

```
      filename = input( 'Please enter filename >', 's' );

      try
        % Calls MOKE function and adds coercivity to the set of
        % points already established.
        coerce = [ coerce , moke(filename) ];
        fileok = 1;    % Sets flag true.
      catch    % If error occurs in loading file.
        disp( ' ' );
        disp( 'File Not Found' );
      end
    end

  % Prompts user for direction of field
  disp( ' ' );
  direct = [ direct, input( 'Please enter direction in degrees >'
                          )
         ];

  elseif option == 2           % “Remove Last Data”
    % Truncates last item in coercivity vector
    coerce = coerce( 1 : length( coerce ) – 1 );
    % Truncates last item in direction vector
    direct = direct(1:length(direct)-1);
    disp( ' ' );
    disp( 'Last Data Removed' );

  elseif option == 3           % “Plot Graph”
    finished = 1;              % Exits menu
  end
end

plot( direct, coerce );    % Plots Coercivity against Direction
disp( ' ' );
title( 'Variation of Coercivity with Magnetic Field Direction' );
xlabel( 'Magnetic Field Direction' );
ylabel( 'Coercivity (kOe)' );
figure( gcf );

% End of Function
```

This function presents the user with a graphical user interface (GUI). Three options are provided:

1) To add a new MOKE data file.
2) To remove the last MOKE data file.
3) To draw a graph of coercivity variation for the MOKE data entered.

When a new file is added, the user specifies the filename either in full or relative to a predefined MATLAB path. The filename must begin with a letter (not a number) for compatibility with naming conventions in MATLAB. The `moke.m` function is called as described above, and the result of the coercivity calculation is stored in a vector. The user is then requested to enter the corresponding direction of the magnetic field. When the user chooses to remove the last data, the coercivity and direction vectors are truncated to remove the last entry.

When the graph-drawing mode is selected, the function plots the coercivity against applied magnetic field direction and applies a suitable title and axis headings. These two MATLAB functions will be equally applicable to any experiment analysing the variation of coercivity with magnetic field direction. It is therefore suggested that a copy of MATLAB be purchased by the Spintronics research group at York and the two m-files implemented as above.

C. Calculation of Resonance Parameters

To facilitate calculation of resonance parameters, a MATLAB function was created and stored in “`resonate.m`”. The user is prompted to input the necessary device parameters and the resulting model parameters are displayed. The resonant frequency and the resistance at resonance are displayed.

```
function [ C , L , Rloss , f0 , Rs] = resonate
% [ C , L , Rloss , f0 , Rs] = RESONATE
%
% Calculates the equivalent circuit parameters and approximates
% the resonant frequency for a hybrid spin-valve with a square
% face.
%
% (c) A Valavanis 2004
```

```
% Prompts user for geometry data and scales variables to the
% required units
disp( ' ' );
disp( 'Device Geometry' );
disp( '---------------' );
disp( ' ' );
h = 1e-6 * input( 'Enter channel thickness in microns >' );
w = 1e-6 * input( 'Enter width of ferromagnetic pads in microns>'
                 );
r = input( 'Enter length of bond wires in mm >' );
disp( ' ' );

% Prompts user for material data and calculates permeabilities
% for metallic layers
disp( 'Top Contact' );
disp( '-----------' );
mu_t = 4e-7 * pi * input( 'Enter relative permeability >' );
sig_t = input( 'Enter conductivity in S/m >' );
disp( ' ' );

disp( 'Bottom Contact' );
disp( '--------------' );

mu_b = 4e-7 * pi * input( 'Enter relative permeability >' );
sig_b = input( 'Enter conductivity in S/m >' );
disp( ' ' );

% Prompts user for material data and calculates permittivity
% for semiconductor channel

disp( 'Channel' );
disp( '-------' );
eps_c = 8.854e-12 * input( 'Enter relative permittivity >' );
sig_c = input( 'Enter conductivity in S/m >' );
disp( ' ' );

% Calculates the equivalent circuit parameters and resonance data
disp( 'Parameter Calculation...' );
C = eps_c * w ^ 2 / h;
L_contact = 2e-9 * r ;
L_device = 4e-7 * pi * h ;
```

```
L = L_contact + L_device ;
Rloss = h / ( sig_c * w ^ 2 );
f0 = 1 / ( 2 * pi * sqrt( L * C ) );
Rs0 = sqrt( f0 * pi ) * ( sqrt( mu_t / sig_t ) + sqrt( mu_b /
sig_b ) );

% Displays the equivalent circuit model parameters.

disp( [ 'Device Inductance = ' , num2str( L_device ) , 'H' ] );
disp( [ 'Packaging Inductance = ' , num2str( L_device ) , 'H' ]
    );
disp( [ 'Total Capacitance = ' , num2str( C ) , 'F' ] );
disp( [ 'Parallel Loss Impedance = ' , num2str( Rloss ) , 'ohm' ]
    );
disp( [ 'Resonant Frequency (approx) = ' , num2str( f0 ) , 'Hz' ]
    );
disp( [ 'Resistance at Resonance (approx) = ' , num2str( Rs0 ) ,
        'ohm'
      ]
    );
% End of function
```

Appendix II. Derivation of Lorenz Force Equation

The Lorenz force is given in section 3.4 as

$$\mathbf{F} = q(\mathbf{E} + \mathbf{u} \times \mathbf{B})$$

Substituting in the equation for total magnetic field due to the spin-orbit interaction given in 3.8 gives

$$\mathbf{F} = q\left(\mathbf{E} + \mathbf{u} \times \left(\mathbf{B_{app}} + \frac{1}{c}(\mathbf{u} \times \mathbf{E})\right)\right)$$

Applying the Distributive Rule for vector multiplication:

$$\mathbf{F} = q\left(\mathbf{E} + \mathbf{u} \times \mathbf{B_{app}} + \frac{1}{c}\mathbf{u} \times (\mathbf{u} \times \mathbf{E})\right)$$

Applying the vector triple product expansion:

$$\mathbf{F} = q\left(\mathbf{E} + \mathbf{u} \times \mathbf{B_{app}} + \frac{1}{c}(\mathbf{u}(\mathbf{u} \cdot \mathbf{E}) - \mathbf{E}(\mathbf{u} \cdot \mathbf{u}))\right)$$

Applying the definition for scalar multiplication:

$$\mathbf{F} = q\left(\mathbf{E} + \mathbf{u} \times \mathbf{B_{app}} + \frac{1}{c}\left(\mathbf{u}(\mathbf{u} \cdot \mathbf{E}) - u^2\mathbf{E}\right)\right)$$

This can be rearranged to give the required complete equation:

$$\mathbf{F} = q\left(\left(1 - \frac{u^2}{c}\right)\mathbf{E} + \mathbf{u} \times \mathbf{B_{app}} + \left(\frac{\mathbf{u} \cdot \mathbf{E}}{c}\right)\mathbf{u}\right)$$

Abbreviations

2DEG	Two-Dimensional Electron Gas
AlGaAs	Aluminium Gallium Arsenide
AMR	Anisotropic Magnetoresistance
ADC	Analogue to Digital Converter
As	Arsenic
CIP	Current In Plane
CMOS	Complementary Metal Oxide Semiconductor
COSHH	Control Of Substances Hazardous to Health
CPP	Current Perpendicular to Plane
FET	Field Effect Transistor
FRAM	Ferrite Random Access Memory
GaAs	Gallium Arsenide
GMR	Giant Magnetoresistance
GUI	Graphical User Interface
H_2O_2	Hydrogen Peroxide
H_2SO_4	Sulphuric Acid
IBM	International Business Machines
IC	Integrated Circuit
IEEE	Institution of Electronic and Electrical Engineers
IPA	Isopropyl Alcohol / Propan-2-ol
LAN	Local Area Network
laser	Light Amplification by Stimulated Emission of Radiation
MOKE	Magneto-Optic Kerr Effect
MOSFET	Metal-Oxide-Semiconductor Field-Effect-Transistor
MRAM	Magnetoresistive Random Access Memory
MTJ	Magnetic Tunnel Junction
NH_4OH	Ammonium Hydroxide
NiFe	Permalloy
NMOS	n-type Metal Oxide Semiconductor
OPC	Optical Proximity Correction
PMOS	p-type Metal Oxide Semiconductor

PSM	Phase Shift Masking
RF	Radio Frequency
RIE	Reactive Ion Etch
rpm	Revolutions Per Minute
Spin-FET	Spin-Transport Field Effect Transistor
Spin-LED	Spin-Transport Light Emitting Diode
Spin-RTD	Spin-Transport Resonant Tunnelling Diode
UV	Ultraviolet radiation
WAN	Wide Area Network

References

---

[1] K E Drexler, “Engines of Creation, The Coming Era of Nanotechnology”, Anchor Books 1986 p216

[2] M R Freeman & B C Choi, “Advances in Magnetic Microscopy”, Science vol 294, 16 Nov 2001, pp1484 - 1487

[3] J F Wakerly, “Digital Design Principles & Practices” 3rd Ed., Prentice Hall, 2001 Sec 1.10

[4] C Edwards, “Cut Price Tricks for Custom-Chip Masks”, IEE Electronics Systems and Software, Feb/ March 2004, pp 10-15

[5] G M Whitesides & J C Love, “The Art of Building Small”, Scientific American, September 2001, pp33-41

[6] M Roukes, “Plenty of Room Indeed”, Scientific American, September 2001, pp42-49

[7] H S P Wong et al, proc. IEEE, vol 87, p537

[8] G Stix, “Little Science”, Scientific American, September 2001, pp26-31

[9] F T Ulaby, “Fundamentals of Applied Electromagnetics”, Prentice Hall, 1999 pp 208-213

[10] P A Tipler & G Mosca, “Physics for Scientists and Engineers”, W H Freeman, 2004

[11] G A Prinz, “Hybrid Ferromagnetic-Semiconductor Structures”, November 1990, Science vol 250

[12] P Evans et al, “Epitaxial Growth and Magnetic Anisotropy of Electrodeposited Ni and Co Thin Films Grown of n-Type GaAs”, IEEE Transactions on Magnetics vol 38 No 5, September 2002 pp 2670-2672

[13] A T Filip, “Spin Polarized Electron Transport in Mesoscopic Hybrid Devices”, University of Groningen, 4 January 2002

[14] National Institute of Standards and Technology: Semiconductor Electronics Division. http://www.eeel.nist.gov/812/effe.htm

[15] Azzopardi & Stewart, “Accessible Physics”, Macmillan, 1995

[16] E I Rashba, “Theory of Electrical Spin Injection: Tunnel Contacts as a Solution of the Conductivity Mismatch Problem”, Physical Review B, vol 62, no 24, pp 267-270, Dec 2000

---

[17] A T Hanbicki et al, “Analysis of the transport process providing spin injection through an Fe/AlGaAs Schottky barrier”, Applied Physics Letters, vol 82, No 23 pp 4092-4094, 9 June 2003

[18] B G Streetman, “Solid State Electronic Devices”, Fourth Edition, Prentice Hall International Editions, 1995

[19] A G Redfield, “On the Theory of Relaxation Processes”, IBM Journal, Jan 1957 pp 19-31

[20] E I Rashba, Soviet Physics Solid State vol. 2, p1109, 1960

[21] S A Wolf et al, “Spintronics: A Spin-Based Electronics Vision for the Future”, Science, 16 November 2001, Vol 294, pp 1488-1495

[22] R K Nesbet, “Theory of spin-dependent Conductivity in GMR Materials”, IBM Journal of Research and Development, Vol 42 No 1, January 1998, pp 53-71

[23] W F Egelhoff et al, Journal of Applied Physics vol 82, p 6142, 1997

[24] S A Wolf & D Treger, “Spintronics: A New Paradigm for Electronics for the New Millennium”, IEEE Transactions on Magnetics, 5 September 2000, Vol 36, No 5, pp 2748 – 2751

[25] G A Prinz, “Magnetoelectronics,” Science, vol 282 pp 1660-1663, Nov 1998

[26] A Fert et al, “The new Era of Spintronics”, Europhysics News 2003, vol 34 no 6

[27] A Tanaka et al, “Top, Bottom, and Dual Spin Valve Recording Heads with PdPtMn Antiferromagnets”, IEEE Transactions on Magnetics, Vol 35, No 2 March 1999, pp700-705

[28] http://hyperphysics.phy-astr.gsu.edu/hbase/tables/curie.html#c1

[29] J Zhu, “MRAM: The Path to Competitiveness”, Presentation given to IEEE Magnetics Society, 21st May 2004.

[30] S Datta & B Das, “Electronic analog of the electro-optic modulator”, Applied Physics Letters, vol 56 (7), pp 665-667, 12 February 1990

[31] B T Jonker et al, “Electrical Spin Injection and Transport in Semiconductor Spintronic Devices”, MRS Bulletin, October 2003 pp 740-747

[32] Y Jiang & M B A Jalil, “Controllable Spin-Filtering and Magnetoconductance in a Novel Hybrid FM/2DEG/FM Structure,” Modern Physics Letters B, Vol 17, Nos 27 & 28, pp1437-1444, 2003

---

[33] G Meier et al, “Field Effect in InAs/ Permalloy hybrid transistors”, Physical Review B, Vol 65, 125327, 2002

[34] F J Jedema et al, “Electrical Spin Injection and Accumulation at Room Temperature in an All-metal Mesoscopic Spin-Valve”, Nature vol 410, 15 March 2001 pp345-348

[35] P R Hammar et al, “Observation of Spin Injection at a Ferromagnet-Semiconductor Interface”, Phys. Review Letters, 1999, Vol 83, No 1, p203

[36] P R Hammar et al, “Hammar et al Reply”, Phys. Review Letters, 2000, Vol 84, No 21. p5024

[37] F Monzon et al, “Magnetoelectric Phenomena at a Ferromagnet-Semiconductor Interface”, Phys. Review Letters, 2000, Vol 84, No 21, p5022

[38] B J Van Wees, “Comment on ‘Observation of Spin Injection ar a Ferromagnet-Semiconductor Interface’”, Phys. Review Letters, 2000, Vol 84, No 21, p5023

[39] S Das Sarma et al, “Theoretical Perspectives on Spintronics and Spin-Polarized Transport”, IEEE Transactions on Magnetics, Vol 36 No 5 September 2000, pp2821-2826

[40] H Ajinaga & H Ohno, “Semiconductor Spintronics”, IEEE Transactions on Nanotechnology, Vol 1 No 1 March 2002, pp19-31

[41] J Nitta et al, Physics Review Letters, vol 78, p1335, 1997

[42] C M Hu, “Spin-Polarized Transport in a two-dimensional electron gas with interdigital-ferromagnetic contacts”, Physical Review B, Volume 63 pp125333-1 – 125333-4

[43] D I Pugh, “The Design and Investigation of Hybrid Ferromagnetic/ Silicon Spin Electronic Devices”, University of York 2001

[44] S Singh, “The Code Book: The Secret History of Codes and Code-Breaking”, Fourth Estate, 1999.

[45] Grey et al, “Analysis and Design of Analog Integrated Circuits”, Fourth Edition, Wiley 2001

[46] G Schmidt et al, “Conductance Mismatch: A Basic Obstacle for Spin Injection in Semiconductors”, Physical Review B vol 62, 2000.

[47] Conversation with Dr M H Capstick, 20/05/04.

[48] A Valavanis, “Spin Electronic Devices – Combine the Hard Disk and the Processor: Initial Report”, University of York, February 2004

---

[49] N I Wright, "Etching and Cleaning Procedures for Semiconductor Materials", University of York, May 1987

[50] INSPEC, "Properties of Gallium Arsenide", 1986

[51] D W Shaw, Journal of the Electrochemical Society Vol 128, 1981, p874

[52] E Ahmad, "Micromagnetism of Epitaxial Ferromagnetic Microelements", University of Cambridge, 1998

[53] The Mathworks Inc. "The Student Edition of MATLAB ®: The Ultimate Computing Environment for Technical Education. Version 4 User Guide", Prentice Hall, 1995

[54] A Cavallo et al, "Using MATLAB: SIMULINK and Control System Toolbox. A Practical Approach", Prentice Hall 1996

[55] "MA 750 Mask Aligner: Technical Manual", Sulzer Electro Technique, 20/11/86

[56] M El-Gomati, 4th Year Course Notes: "Electron Devices, Growth and Characterisation", University of York 2003

[57] S S Hees, "Nanomagnetic FET for Spin Electronics and Information Storage", University of York, June 2003

[58] S Clements, Presentation given at IOP site visit to Filtronics PLC, 6th May 2004